J. Fluid Mech. (2009), *vol.* 630, *pp.* 5–41. © 2009 Cambridge University Press
doi:10.1017/S0022112009006624 Printed in the United Kingdom

Direct numerical simulation of turbulence in a nominally zero-pressure-gradient flat-plate boundary layer

XIAOHUA WU[1] AND PARVIZ MOIN[2]†

[1]Department of Mechanical Engineering, Royal Military College of Canada, Kingston, Ontario, Canada K7K 7B4
[2]Centre for Turbulence Research, Stanford University, Stanford, CA 94305-3035, USA

(Received 3 October 2008 and in revised form 4 February 2009)

A nominally-zero-pressure-gradient incompressible boundary layer over a smooth flat plate was simulated for a continuous momentum thickness Reynolds number range of $80 \leqslant Re_\theta \leqslant 940$. Transition which is completed at approximately $Re_\theta = 750$ was triggered by intermittent localized disturbances arising from patches of isotropic turbulence introduced periodically from the free stream at $Re_\theta = 80$. Streamwise pressure gradient is quantified with several measures and is demonstrated to be weak. Blasius boundary layer is maintained in the early transitional region of $80 < Re_\theta < 180$ within which the maximum deviation of skin friction from the theoretical solution is less than 1 %. Mean and second-order turbulence statistics are compared with classic experimental data, and they constitute a rare DNS dataset for the spatially developing zero-pressure-gradient turbulent flat-plate boundary layer. Our calculations indicate that in the present spatially developing low-Reynolds-number turbulent flat-plate boundary layer, total shear stress mildly overshoots the wall shear stress in the near-wall region of 2–20 wall units with vanishing normal gradient at the wall. Overshoots as high as 10 % across a wider percentage of the boundary layer thickness exist in the late transitional region. The former is a residual effect of the latter. The instantaneous flow fields are vividly populated by hairpin vortices. This is the first time that direct evidence (in the form of a *solution* of the Navier–Stokes equations, obeying the statistical measurements, as opposed to synthetic superposition of the structures) shows such dominance of these structures. Hairpin packets arising from upstream fragmented Λ structures are found to be instrumental in the breakdown of the present boundary layer bypass transition.

1. Introduction

Turbulent spatially developing zero-pressure-gradient incompressible boundary layer over a smooth flat plate (ZPGFPBL) is an important problem in modern fluid mechanics. Numerous experimental and theoretical studies on the statistics and structures of turbulent ZPGFPBL are available in the literature dated as early as Coles (1956), Favre, Gaviglio & Dumas (1957), and as recent as Hutchins & Marusic (2007), Monkewitz, Chauhan & Nagib (2007). Hutchins and Marusic studied the large-scale coherent structures in the logarithmic region while Monkewitz *et al.* focused on the

† Email address for correspondence: moin@stanford.edu

scaling of mean velocity profile at high-Reynolds-number regime. One of the principle reasons that these studies were possible is that turbulent ZPGFPBL can be routinely realized in wind tunnels at different laboratories with flush-mounted trip wire for the promotion of boundary layer transition and with flexible roof for the control of streamwise pressure gradient, yielding quality data for theoretical analysis.

In contrast to the abundance of experimental data on the turbulent ZPGFPBL, there exist very few high-quality DNS datasets, regardless of the Reynolds number regime. In fact, two decades after the publication of the ground-breaking paper by Spalart (1988), his statistics remain the only widely accepted DNS dataset on the turbulent ZPGFPBL. The scheme of Spalart (1988) is elaborate and involves a set of debatable approximations in order to apply the numerically convenient periodic boundary condition in the streamwise direction. It is interesting to note that the turbulent channel flow DNS of Kim, Moin & Moser (1987), published at about the same time, has been reproduced many times by various groups around the world for purposes of turbulence physics investigation as well as model development. As a result there exists little controversy regarding the true values of mean and second-order statistics for the channel flow over the low-to-intermediate Reynolds number range. The same cannot be said for the turbulent ZPGFPBL. Honkan & Andreopoulos (1997) compared the second-order turbulence statistics reported by 11 groups on turbulent ZPGFPBL, with Spalart's results again being the only DNS ZPGFPBL dataset in the entire compilation. The figures presented by Honkan and Andreopoulos demonstrate considerable scatter in the profiles of all the Reynolds stress components from various groups especially in the near-wall region even at very similar Reynolds numbers. Given the fundamental importance of the turbulent ZPGFPBL and the sharp status disparity between the advanced laboratory measurements and the rather limited success of DNS, there is a compelling reason to revisit the DNS of spatially developing turbulent ZPGFPBL. This undertaking also brings in the companion issue of bypass transition in the ZPGFPBL. Analogous to the situation of turbulent ZPGFPBL, there exist very few solid reproducible DNS statistics that can be used for modelling and theoretical analysis on the transitional ZPGFPBL even though in this case computationally generated structural information is abundant.

1.1. *Previous DNS of turbulent ZPGFPBL*

The pioneering work of Spalart (1988) simulated a quasi-ZPGFPBL at four discrete momentum thickness Reynolds numbers, $Re_\theta = 225$, 300, 670 and 1410. Streamwise growth of the boundary layer was approximated with a multiple-scaling procedure. This procedure involves approximate treatment of the dependent and independent variables as well as approximate treatment of the Navier–Stokes equations. A new coordinate replaces the wall-normal coordinate along which boundary layer thickness and viscous sublayer thickness are assumed to be constant with respect to streamwise distance. It was argued that this is a weak assumption and can only have an indirect effect on the results. Dependent variables are treated with a set of much more involved decomposition and transformation procedures in order to make the use of periodic condition for the fluctuating signals tolerable. The Navier–Stokes equations and the continuity equation are also transformed accordingly. In the final equation set, corrections in the viscous terms are neglected, and straining of turbulence by the mean flow is not accurately represented.

Khurajadze & Oberlack (2004) simulated a flat-plate boundary layer at Re_θ up to 2500 with periodic boundary condition in the streamwise direction. To overcome

the difficulties associated with non-physical streamwise periodicity, a fringe region technique was used. The method rescales the boundary layer growth normal to the wall. In this way the physical domain and the fringe region together satisfy the streamwise periodic boundary conditions. An extra forcing function was added to the Navier–Stokes equations in the fringe region which is non-zero only in this region. At the exit of the computational domain the flow was forced back to be laminar. Their simulations started with a laminar boundary layer as inflow which was triggered to transition by adding a random volume force term to the Navier–Stokes equations near the wall.

There is a large body of published work on generating turbulent inflow boundary condition for simulation of complex spatially developing external flows; the most representative paper is perhaps that of Lund, Wu & Squires (1998). Lund *et al.* (1998) developed a simplified version of the Spalart method by invoking only the transformation on independent variables at two streamwise stations without altering the Navier–Stokes equations. This method and its subsequent variations have been shown to yield reasonable inflow conditions for complex spatially developing flows because quite often the downstream pressure gradients and geometrical variations mask any major defects of the inflow. However, because of their semi-empirical nature, even with DNS resolution, it would be quite challenging for these methods to generate results that can be considered as experimental data quality for the turbulent ZPGFPBL.

In recent years, it has become evident that certain important behaviours of simple flow statistics such as the mean velocity profile have not been well understood (Barenblatt & Chorin 1998). Zagarola & Smits (1998) proposed a new scaling law for the mean flow profiles in the turbulent ZPGFPBL. They expressed doubts about the existence of any universal overlap region for boundary layers with $Re_\theta < 1800$. They conjectured that for inner variable scaling a log-law velocity profile can exist only for $Re_\theta > 3000$, contrary to the scaling formulas assumed in many of the inflow generation and rescaling schemes. A power-law dependence of u^+ on y^+ was proposed for the mean velocity profile in the intermediate-Reynolds-number range. When normalizing the wall-normal position in the outer region, boundary layer thickness δ was used. Regardless of the length scale used, they found that the collapse of u^+ or u/U_∞ profiles from different Reynolds numbers was poor in the outer region. However, when the velocity profiles were normalized by a new velocity scale $U_\infty \delta^*/\delta$, the collapse was much improved in the outer region; here δ^* is the boundary layer displacement thickness. DeGraaff & Eaton (2000) did extensive high-resolution measurements in a low-speed high-Reynolds-number facility on the turbulent ZPGFPBL from $Re_\theta = 1430$ to 31 000. They found that the streamwise Reynolds stress $\overline{u'^2}$ did not scale on u_τ^2 even in the near-wall region though the wall-normal Reynolds stress $\overline{v'^2}$ and the Reynolds shear stress collapse well with u_τ^2 at $Re_\theta > 2000$. They proposed a new mixed scale for the streamwise Reynolds stress component. For a review of recent progress on mean velocity scaling, see Monkewitz *et al.* (2007).

The works of Zagarola & Smits, DeGraaff & Eaton and Monkewitz *et al.* and references therein on the scaling of mean and second-order statistics in the turbulent ZPGFPBL reinforce our notion that fine-resolution simulations incorporating scaling arguments into their inflow generation scheme impose a bias in the generated numerical results. This is because it is precisely these scaling behaviours that are at the centre of debate in recent experimental and theoretical studies on turbulent ZPGFPBL.

1.2. *Previous DNS of transitional ZPGFPBL*

A straightforward way to compute a turbulent ZPGFPBL is to promote the transition of an upstream Blasius boundary layer, preferably through a mechanism which bypasses the extremely slow Tollmien–Schlichting route (Rai & Moin 1993). This is in the same spirit as the routine procedure of mounting trip wires in wind tunnel experiments. Reasonably successful attempt at taking the incompressible ZPGFPBL from Blasius to turbulent flow through bypass transition using DNS was first achieved by Wu *et al.* (1999), followed later by Jacobs & Durbin (2001). These full boundary layer bypass transition simulations are important because of their relevance to turbomachinery applications where upstream blade row wakes trigger transition on the downstream blades, and because of their marked departure from traditional computational approaches to transition.

More recent boundary layer bypass transition computations were reported by Brandt, Schlatter & Henningson (2004), Zaki & Durbin (2005) and Ovchinnikov, Piomelli & Choudhari (2006). However, these three studies focused almost exclusively on the issue of bypass transition mechanism. Their boundary layers did not attain a genuine turbulent ZPGFPBL state from which quality turbulent ZPGFPBL statistical data could be extracted.

Wu *et al.* (1999) computed a ZPGFPBL from $Re_\theta = 80$ to 1120 on 50 million grid points. The boundary layer transitioned due to perturbations associated with migrating wakes introduced periodically at the inlet. The inlet wakes were generated from a separate temporally decaying wake simulation, and they slid through the inlet plane along the wall-normal direction at a prescribed frequency. Turbulent statistics show good comparison with those from Spalart (1988) inside the boundary layer, although the primary interest and contribution of that study was in studying how infant turbulent spots were generated in bypass transition. The migrating wakes produced mean flow distortions even in the free stream which affected turbulence statistics in the outer region. The imposed inflow condition was less ideal in the sense that the inlet wake distortion on the Blasius boundary layer was prescribed in an artificial manner. Only 1024 grid points were applied along the streamwise direction.

Jacobs & Durbin (2001) computed a ZPGFPBL for a momentum thickness Reynolds number range of $120 \leqslant Re_\theta \leqslant 1000$ on 70 million grid points. At the inlet isotropic turbulence was introduced continuously from both inside and outside the Blasius boundary layer. Their isotropic turbulence was generated as a sum of Fourier modes. Similar to the work of Wu *et al.* (1999), Jacobs & Durbin (2001) concentrated on investigating the breakdown mechanism in bypass transition. Although their streamwise turbulence intensity showed good agreement with the experimental data of Roach & Brierley (1990), there were noticeable discrepancies in all the other turbulent stress components. Neither the turbulent statistics sampled by Wu *et al.* (1999) nor those of Jacobs & Durbin (2001) can be considered as experimental data quality for the turbulent ZPGFPBL. Comparison of the turbulence statistics with experiments in those studies was merely used to show that the transition was complete. The only widely adopted dataset for boundary layer bypass transition modelling is from the experimental work of Roach & Brierley (1990). Thus, aside from the need for a genuine spatially developing turbulent ZPGFPBL simulation for turbulent statistics, there is also a strong motivation to design and execute a benchmark-quality DNS with well defined and reproducible inflow conditions to obtain flow statistics in the transitional regime.

This paper reports our numerical simulation of a nominally ZPGFPBL from the Blasius regime through transition to turbulence. Our approach is genuinely spatially developing: without either invoking the non-physical streamwise periodicity or adding terms to the Navier–Stokes equations. Two primary objectives were to obtain a DNS dataset for the turbulent ZPGFPBL that is of experimental data quality, and to acquire a well-documented and reproducible statistical dataset for boundary layer bypass transition that is of value to modellers. Bypass transition mechanism has also been investigated. Time-dependent dynamics of turbulence structures are not dealt with in this paper, although a set of instantaneous visualization images with striking clarity is presented which provides new insight into the structure of turbulent boundary layer.

2. Computation details

Several factors were taken into account in designing the simulation. Given a sufficiently strong finite amplitude perturbation, a laminar boundary layer rapidly becomes turbulent. However, the final state of the resulting turbulent boundary layer may not be a realization of the genuine ZPGFPBL if the transition process is not well controlled: the streamwise pressure gradient may deviate substantially from zero; the convected finite amplitude perturbations may markedly alter the state of the downstream flow both inside and outside the boundary layer; perturbations may be high enough to render linear theory inapplicable; the strong disturbances may even eliminate the early transitional region which in turn makes it impossible to study the process of breakdown. Ideally, one should introduce a numerical 'trip wire' capable of promoting bypass transition through weak disturbances which at the same time leaves well-defined faint footprints on the downstream boundary layer.

Consider the development of an incompressible initially laminar boundary layer flowing over a smooth flat plate with upstream patches of isotropic turbulence passing periodically as shown in figure 1. The target streamwise pressure gradient is zero throughout the computational domain, but this is not achieved precisely in the simulation. This design has its root in the passing wake simulation of Wu *et al.* (1999). Here, the main concerns are to minimize streamwise pressure gradient, and to reduce disturbance to the boundary layer. This simulation design should be easily reproducible by other groups with DNS, LES or URANS.

At the inlet station, a Blasius boundary layer of momentum thickness Reynolds number $Re_\theta = 80$ is prescribed. The characteristic length scale is based on the inlet-boundary-layer momentum thickness $\theta_0 = 1$. The origin of the Cartesian system is located on the wall at the inlet station. The computational domain is $0 \leqslant x/\theta_0 \leqslant 6375$ in the streamwise direction, $0 \leqslant y/\theta_0 \leqslant 1500$ in the wall-normal direction and $0 \leqslant z/\theta_0 \leqslant 375$ along the spanwise direction. Characteristic velocity scale is the constant free stream velocity $U_\infty = 1$. Unless otherwise stated, all the coordinates are normalized by the characteristic length scale inlet-boundary-layer momentum thickness θ_0. The spanwise dimension of the computational domain is equivalent to approximately 3.5δ near the exit, where δ is the local boundary layer thickness. This should be adequate in ZPGFPBL simulations because the spanwise scale of even the largest eddies in a turbulent ZPGFPBL is generally considered as to be less than δ (for example, see Tomkins & Adrian 2003). Our spanwise two-point correlation coefficients collected at $Re_\theta = 900$ (not shown here) also confirm that the width of the computational domain is adequate.

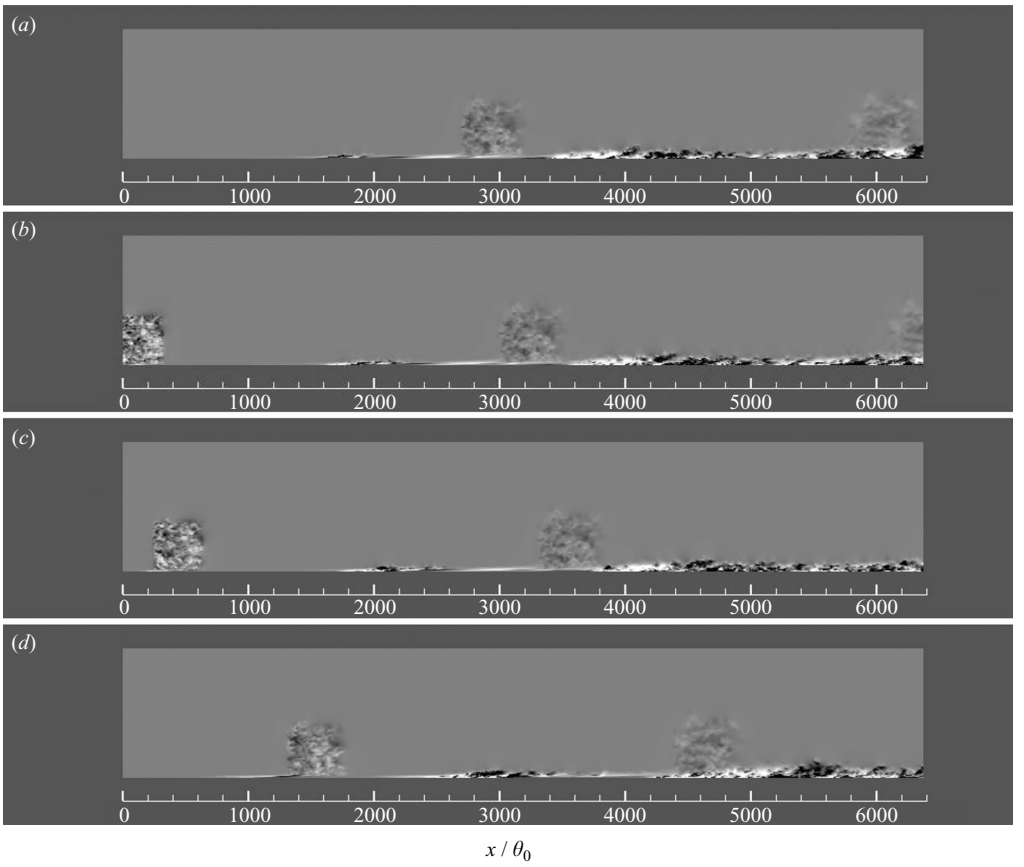

FIGURE 1. Contours of v' over one xy-plane at four consecutive instants. (a) $100\mathscr{T}$; (b) $100.1\mathscr{T}$; (c) $100.2\mathscr{T}$; (d) $100.55\mathscr{T}$. White and black colours represent stronger positive and negative values of v', respectively. v'/U_∞ varies from -0.08 to 0.08. The images' horizontal (x) to vertical (y) aspect ratio is 1:1 so that the x-axis tick marks can be directly applied to the y-axis.

At the inlet, patches of isotropic turbulence were introduced at a prescribed frequency $\mathscr{T}$ (see figure 1). Each patch is a slab with dimensions of $375\theta_0$ in each direction, the same as the spanwise dimension of the boundary layer simulation. We use 'slab' here to emphasize that the patch extends across the entire spanwise direction, notwithstanding that the real configuration of the turbulent patch is a cube.

The isotropic velocity fluctuations have been obtained from a separate DNS computation of homogeneous, decaying turbulence provided by Dr Alan Wray, NASA Ames. This DNS was carried out with a spectral code in a periodic computational cubic box on a 512^3 mesh. The initial spectrum is of the type $E(k) \sim k^4 \exp(-bk)$. The velocity field corresponds to the instant at which the energy has decayed by 50 % and the skewness has become roughly constant (A. Wray 2008, personal communication). At this particular instant, squares of the r.m.s. intensities of the three velocity components are 0.039, 0.041 and 0.039, respectively. In the conversion to real space, the spectral data for the higher frequencies have been filtered to reduce the data to 256^3 of Fourier modes. One-dimensional spectra of the isotropic turbulent flow velocity components as a function of wavenumber k_x are shown in figure 2. Longitudinal (f)

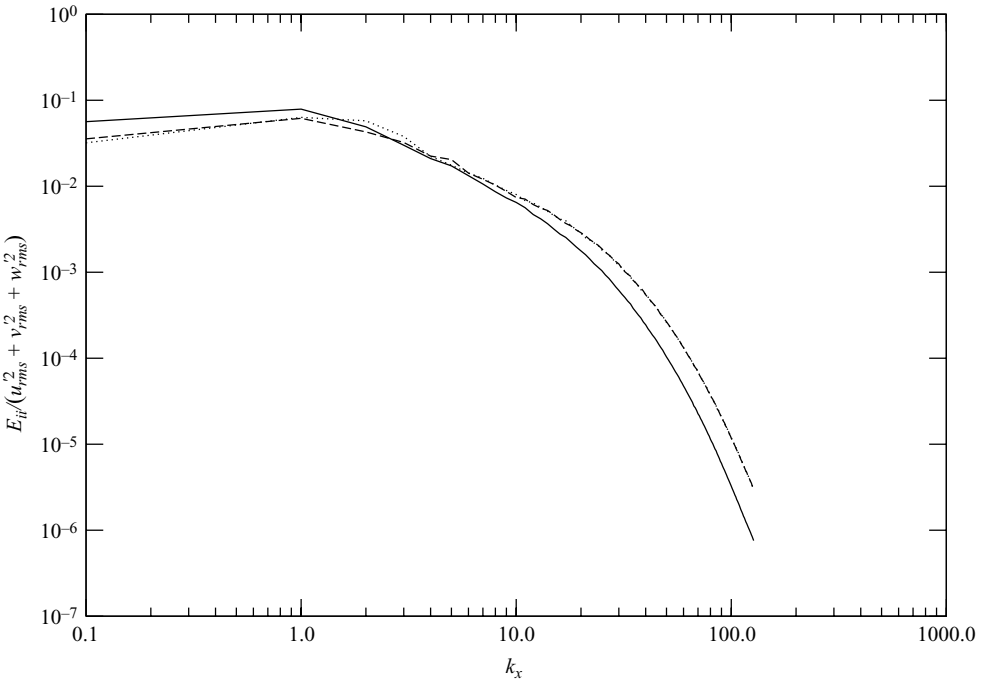

FIGURE 2. One-dimensional spectrum of inflow isotropic turbulence as a function of wavenumber k_x. Solid line, E_{uu}; dotted line, E_{vv}; dashed line, E_{ww}; spectrum normalized by $(u'^2_{rms} + v'^2_{rms} + w'^2_{rms})$ and length of the isotropic turbulence cubic box.

and transverse (g) two-point correlations of the velocity field agree with the theoretical relationship $g = f + 0.5r\,\mathrm{d}f/\mathrm{d}r$.

Turbulence intensities of the isotropic turbulence slab relative to the present free stream velocity U_∞ in the x, y, z directions were 0.0594, 0.0609, 0.0594, respectively. The velocity field of the isotropic turbulence box was introduced into the boundary layer simulation through the free stream at the inlet station periodically. At the initial instant $t = 0$, the box starts to enter the computational domain from $x = 0$ with the streamwise velocity $U_{box} = U_\infty$. Along the wall-normal direction, the box is located in the region $15 \leqslant y/\theta_0 \leqslant 390$; that is, the bottom plane of the isotropic turbulence slab is two-boundary-layer thicknesses away from the wall at the inlet station. In this manner, the Blasius boundary layer at the inlet is undistorted by the imposed perturbations which avoids the arbitrariness inherent in prescribing perturbed velocity profiles inside the layer. At the inlet, $x = 0$, the isotropic turbulent velocity field is simply superimposed on the uniform free stream velocity. The passing period $\mathscr{T}$ is set to be $3131.45\theta_0/U_\infty$ in the present simulation, the same as in Wu *et al.* (1999). Thus, at $t = 3131.45$ or at any integer multiple of $\mathscr{T}$, there is another isotropic turbulence slab entering the inlet plane. The same isotropic turbulent slab is recycled at each new period.

The upper boundary of the present computational domain is located at $y = 1500\theta_0$ or 200 inlet boundary layer thicknesses away from the wall. This is necessary and significantly higher than that in most previous boundary layer simulations. At the top surface of the domain, the following boundary conditions were applied: $v = V_{Blasius}$, $\partial u/\partial y = \partial v/\partial x$, and $\partial w/\partial y = \partial v/\partial z$, corresponding to zero vorticity components.

Since a large streamwise extent of the domain is transitional, prescribing the analytical profile of $v = V_{Blasius}$ at the top surface is reasonable. The alternative of obtaining the v profile at the top boundary using the gradient of δ^* requires either prior knowledge of boundary layer growth and transition location or some tedious iterative procedure. In any case, as clearly demonstrated by figures 6 and 7, our boundary condition in conjunction with the large distance between the top boundary and the wall yields a nominally zero streamwise pressure gradient. At the exit plane of the computational domain $x = 6375\theta_0$, convective boundary conditions were used (Pauley, Moin & Reynolds 1990). Mass flux at the inflow plane was made constant in time by rescaling the velocities, and corrections to the velocities at the exit plane were also made to ensure global mass conservation. Periodic boundary conditions were applied in the homogeneous spanwise z-direction; no-slip condition was applied on the flat plate.

The finite-difference grid size is $4096 \times 400 \times 128$ along the x, y and z directions, respectively. Simulation with a coarser grid of $2048 \times 400 \times 128$ was also performed but not presented in this paper. We found that the profile of the skin-friction coefficient C_f obtained from the coarse grid calculation agreed with that from the fine grid to within 0.5 % for the turbulent region $730 < Re_\theta < 930$. Agreement is also excellent in the early transitional region for $80 < Re_\theta < 170$, with a maximum deviation of less than 0.05 %. However, the minimum C_f is attained at $Re_\theta = 230$ for the coarse grid simulation and at $Re_\theta = 270$ for the fine grid simulation. The present total of 210 million grid points is nearly four times larger than that used by Wu *et al.* (1999) and nearly three times larger than that by Jacobs & Durbin (2001). Grid spacings in the streamwise and spanwise directions were $\Delta x = 1.5563\theta_0$ and $\Delta z = 2.93\theta_0$, respectively. Using the highest computed friction velocity $u_\tau = 0.0475$ in the turbulent region, these spacings can be expressed in wall units as $\Delta x^+ = 5.91$ and $\Delta z^+ = 11.13$, respectively. The spacing in the x-direction is kept small since our previous work on bypass transition simulations has indicated that inadequate streamwise resolution can have a noticeable effect on the flow statistics. This is understandable because, in a boundary layer bypass transition simulation, one needs to resolve not only the near-wall boundary layer flow but also the free stream disturbance. The current Δx^+ value of 5.91 is one of the lowest values that have been used in transitional and turbulent boundary layer simulations. The minimum grid spacing in the wall-normal direction is $\Delta y = 1.3688\theta_0$, and the maximum spacing is $\Delta y = 10.872\theta_0$. In the turbulent region at $x = 5981\theta_0$, $Re_\theta = 900$, there are 10 points below $y^+ = 5$, 18 points below $y^+ = 10$ and 175 points inside the boundary layer. In the transitional region (at $x = 895\theta_0$, $Re_\theta = 200$) close to the breakdown position, there are 80 points inside the boundary layer. In the early transitional region at $x = 97.5\theta_0$, $Re_\theta = 100$, there are 50 points distributed inside the boundary layer along the wall-normal direction.

The time advancement method used to solve the unsteady three-dimensional constant density Navier–Stokes and continuity equations is the fractional step method. Convection and diffusion terms that involve only derivatives in the wall-normal direction are treated implicitly, whereas all other terms are treated explicitly. Velocity components are staggered with respect to pressure. Conservation of kinetic energy in the inviscid limit by the numerical scheme is achieved with the use of staggering. All spatial derivatives are approximated with a second-order central difference scheme. A third-order Runge–Kutta scheme is used for terms treated explicitly and a second-order Crank–Nicolson scheme is used for terms treated implicitly. Scalable parallelization is achieved using message passing interface (MPI). Details of the algorithm were described in Pierce & Moin (2001, 2004). The simulation was

performed using 1024 processors on 128 IBM 8-way P655+ nodes. The computational time step was fixed at $\Delta t = \mathscr{T}/2000$. The maximum component Courant-Friedrichs-Lewy (CFL) number defined as $\Delta t(|u|/\Delta x + |w|/\Delta z)$ was approximately 1.35. Note that the wall-normal direction is treated implicitly. The initial velocity field was prescribed as the Blasius profile. The flow was allowed to evolve from the initial state for $100\,000\Delta t$ (50 passing period $\mathscr{T}$) to reach statistically steady state. Statistics were then collected for another $100\,000\Delta t$. In addition to averaging in time, the statistical sample was enhanced by averaging in the homogeneous spanwise direction.

3. Results

3.1. *Visualizations*

Figure 1 shows images of the present boundary layer using contours of wall-normal fluctuating velocity component v' over one xy-plane at four sequential instants: $100\mathscr{T}$, $100.1\mathscr{T}$, $100.2\mathscr{T}$ and $100.55\mathscr{T}$. Note that the isotropic turbulence slab enters the inflow station every $\mathscr{T} = 2000\Delta t$. At the first instant, $t = 100\mathscr{T}$, the isotropic turbulence slab starts to enter the computational domain from $x = 0$. It takes $240\Delta t$ for the slab to get completely inside the domain. Sections of laminar, transitional and turbulent boundary layer can be clearly seen in the figure. In the snapshot at $t = 100\mathscr{T}$, a turbulent patch can be observed centred around $x = 1700\theta_0$, which has been induced probably by the passage of the isotropic turbulence slab centred around $x = 2950\theta_0$.

In figure 3, six three-dimensional subimages extracted from the velocity field at the single instant of $t = 100.2\mathscr{T}$ are presented, each focusing on a specified streamwise zone showing the iso-surfaces of the second invariant of the instantaneous velocity gradient tensor $\boldsymbol{Q}$ at an approximately zero constant value (Hunt, Wray & Moin 1988). Chakraborty, Balachandar & Adrian (2005) compared several prevailing vortex identification criteria including that of Hunt *et al.* They found that all the criteria result in remarkably similar looking vortical structures. Figure 3(*a*) shows the introduced isotropic turbulent slab near the inlet; an induced Λ-shaped structure near the wall is also visible. In the lower-middle xy-plane image of figure 1 ($t = 100.2\mathscr{T}$), a turbulent patch can be seen in the region of $1800\theta_0 < x < 2600\theta_0$. Figure 3(*b*) clearly shows that this patch actually consists of two turbulent spots. The spots are packed with hairpin vortices of different sizes, and some of the hairpins near the trailing tip of the spots are quite small. Figure 3(*c*) shows vortex structures in the region of $2625\theta_0 < x < 3562\theta_0$ behind the turbulent slab centred at $x = 3562\theta_0$ at this instant. In the middle of this image, a longitudinal structure is surrounded by several incomplete hairpin vortex structures distributed along the streamwise direction. Figures 3(*d*), 3(*e*) and 3(*f*) show vortex structures of the ZPGFPBL at this particular instant in the late transitional regions of $3562\theta_0 < x < 4500\theta_0$, $4500\theta_0 < x < 5437\theta_0$ and in the turbulent region of $5437\theta_0 < x < 6375\theta_0$, respectively.

The preponderance of hairpin-like structures is striking. Although a number of investigators have postulated the existence of such structures in turbulent shear flows (Perry & Chong 1982; Moin & Kim 1985; Adrian, Meinhart & Tomkins 2000; Tomkins & Adrian 2003; Hutchins, Hambleton & Marusic 2005), such a direct evidence for their dominance has not been reported in any numerical or experimental investigation of turbulent boundary layers since the flow visualization experiments of Head & Bandyopadhyay (1981). In contrast to the present results, it has also been reported that complete quasi-symmetric hairpin vortices are rarely observed in turbulent boundary layers (Robinson 1991).

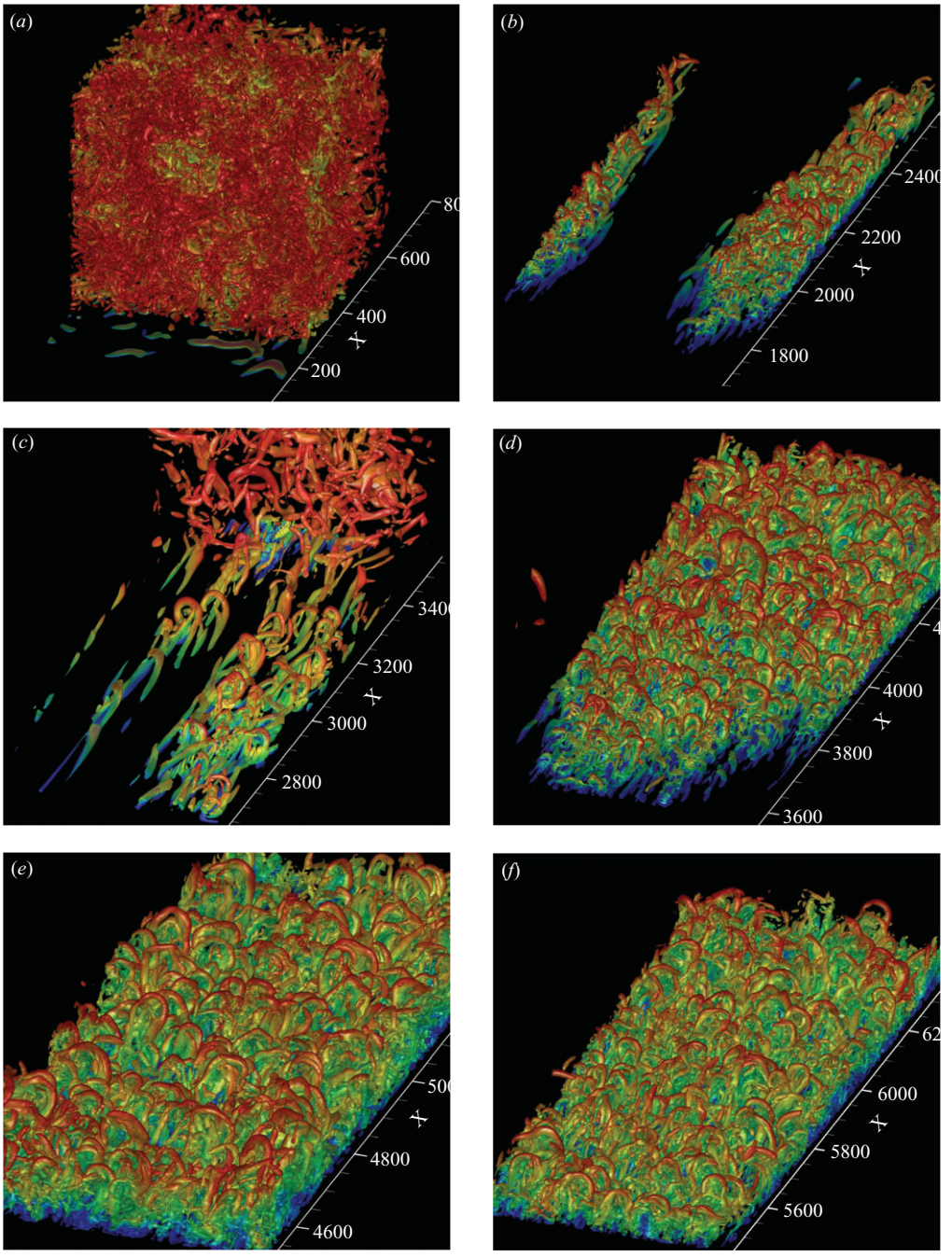

FIGURE 3. Iso-surfaces of the second invariant of the velocity gradient tensor at $t = 100.2\mathscr{T}$. The iso-surfaces are coloured based on local values of u with higher u represented by red, $0 \leqslant u \leqslant 1.0$. Six simultaneous sub-images were taken at this instant focusing on different streamwise zones. x is normalized by the characteristic length scale inlet-boundary-layer momentum thickness θ_0. (*a*) $0 < x < 750$, (*b*) $1687 < x < 2625$, (*c*) $2625 < x < 3562$, (*d*) $3562 < x < 4500$, (*e*) $4500 < x < 5437$; (*f*) $5437 < x < 6375$.

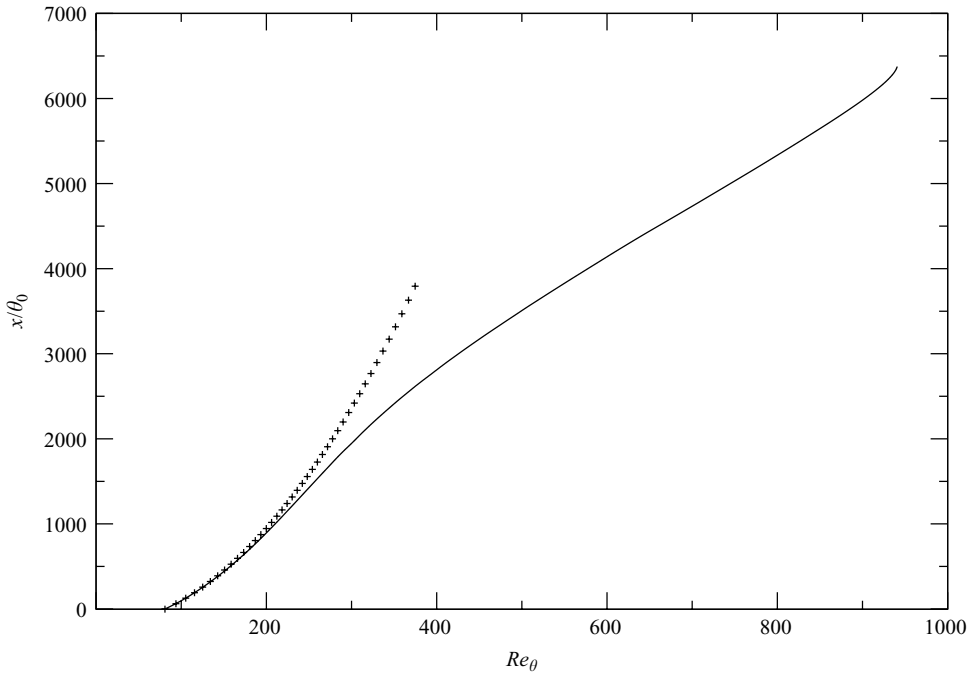

FIGURE 4. Variation of Re_θ with streamwise distance x/θ_0. Solid line, present DNS; plus, Blasius solution.

This is the first time that direct evidence (in the form of a *solution* of the Navier–Stokes equations, obeying the statistical measurements, as opposed to synthetic superposition of the structures) shows such dominance of these structures. Therefore, we believe that preponderance of 'forests' of hairpins (Perry & Chong 1982) in turbulent boundary layer is a credible conceptual reduced-order model of turbulent boundary layer dynamics. The primary reason that previous simulations did not see this dominance might be related to the particular imposition of the boundary conditions. For example, streamwise periodicity in channel flows (and scaled periodicity of Spalart's simulations) lead to a reintroduction of the hairpins at the inflow, which would interact with the structures in the domain resulting in their distortions. Furthermore, in the present simulations, instabilities on the wall were triggered from the free stream, and not by trips or other artificial numerical boundary conditions. It should be noted that the use of smoke in flow visualizations of Head & Bandyopadhyay (1981) resulted in a striking but indirect demonstration of the presence of hairpin vortices. In addition, the relatively large trips used in their tunnel may lead one to speculate that hairpins were actually put in their flow, and did not evolve naturally and owing to flow instabilities. This finding strongly suggests that a study on the time-dependent dynamics of the turbulent ZPGFPBL using the present approach will be valuable. In the remainder of this paper, we mainly focus on the study of time-independent boundary layer statistics.

3.2. *Global statistics*

Figure 4 shows the variation of Re_θ with streamwise distance x. For instance, $Re_\theta = 200$ is located at $x = 895\theta_0$, and $Re_\theta = 900$ is located at $x = 5981\theta_0$. Boundary

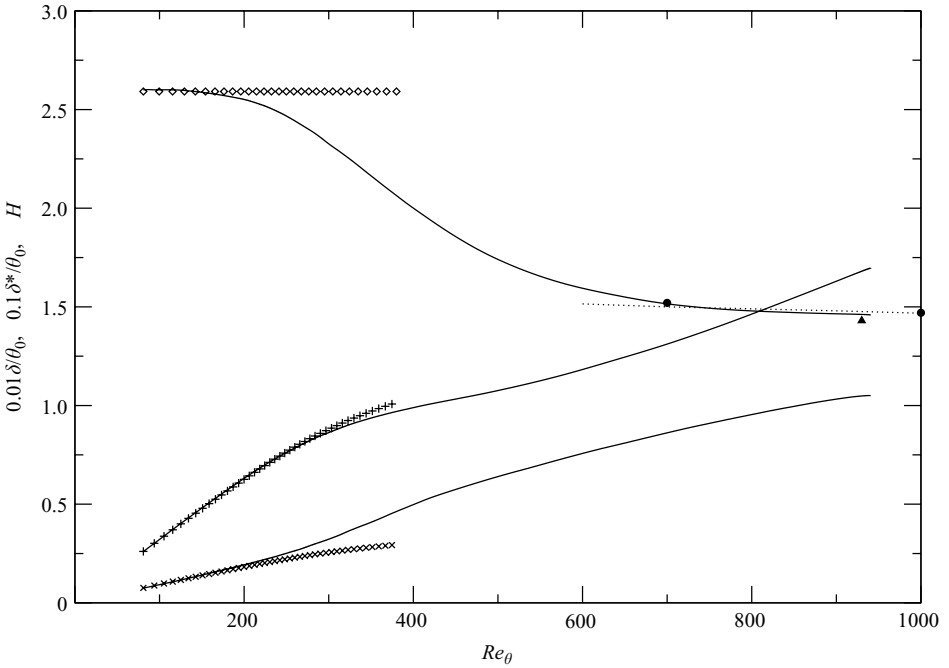

FIGURE 5. Mean boundary layer integral parameters as a function of Re_θ, corresponding x locations can be found in figure 4. Present DNS: solid line. Blasius solutions: cross, boundary layer thickness $0.01\delta/\theta_0$; plus, displacement thickness $0.1\delta^*/\theta_0$; diamond, shape factor H. Dotted line, Nagib *et al.* (2007). Experimental data: circle, Murlis *et al.* (1982); triangle, Adrian *et al.* (2000).

layer integral parameters are presented in figure 5. The boundary layer thickness based on 99 % of the constant free stream velocity U_∞ is $7.5\theta_0$ at the inlet and reaches $105\theta_0$ at $Re_\theta = 900$, a 14-fold increase. This reinforces the need to have the computational domain's upper domain boundary located sufficiently away from the wall. Although the current upper boundary is 200δ away from the wall at the inlet, it is merely 14δ away from the wall at the exit. Although Re_θ, δ and C_f all have departed from their corresponding Blasius solution by $x = 895\theta_0$ or $Re_\theta = 200$, the displacement thickness δ^* remains close to the Blasius solution at least until $Re_\theta = 280$. Thus, δ^* is not a sensitive measure of a boundary layer's departure from Blasius. On the other hand, the shape factor $H = \delta^*/\theta$ is an excellent indicator of the boundary layer state. Figure 5 suggests that in the early transitional region there is good agreement between the computed shape factor and the Blasius solution. By $Re_\theta = 180$ the boundary layer has moved substantially away from the laminar solution. The late transitional region is marked by a large streamwise gradient of H. By $Re_\theta = 750$, the variation of H with streamwise distance begins to level off substantially, suggesting that transition is complete and the flow can be considered as turbulent. In the turbulent region, the present shape factor agrees well with the experimental measurements and the analytical curve of Nagib, Chauhan & Monkewitz (2007).

The dominating effect of the streamwise pressure gradient on boundary layer development was recognized early by Schubauer & Skramstad (1947). When the streamwise pressure gradient deviates from nominally zero, other effects are often overwhelmed and become secondary and less important. It is therefore crucial

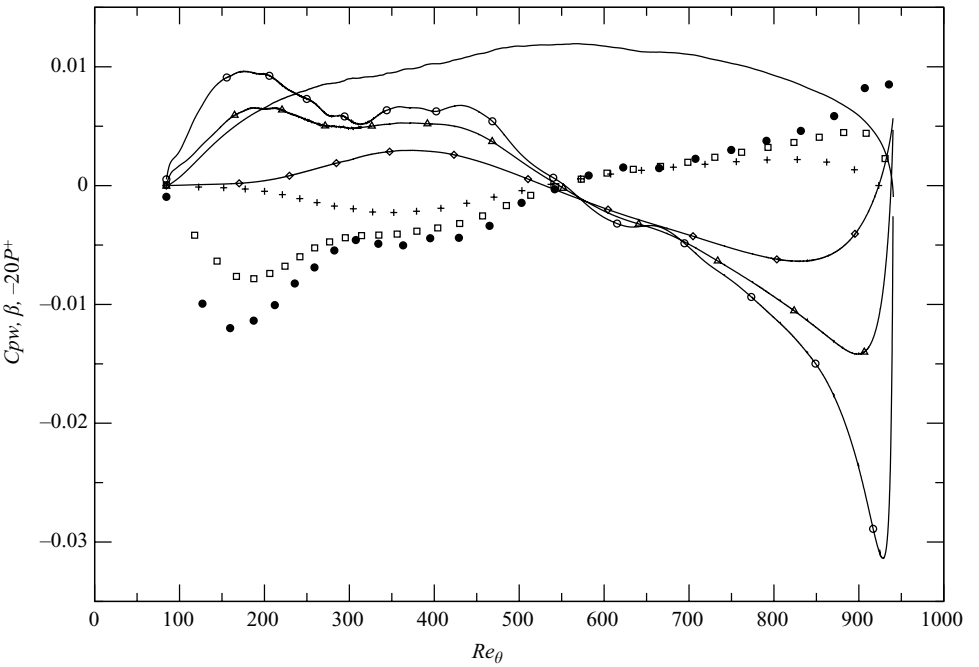

FIGURE 6. Mean streamwise pressure gradients as a function of Re_θ. Solid line without symbol: wall static pressure coefficient C_{pw}; solid line with symbols: open circle, $\beta = (\delta^*/\tau_w)(\partial \bar{p}/\partial x)$ at $y = 187.5\theta_0$; triangle, β at $y = 375\theta_0$; diamond, β at $y = 750\theta_0$; symbols without line: solid circle, $-20P^+ = (\nu/\rho u_\tau^3)(\partial \bar{p}/\partial x)$ at $y = 187.5\theta_0$; square, $-20P^+$ at $y = 375\theta_0$; plus, $-20P^+$ at $y = 750\theta_0$.

for numerical simulations on transitional or turbulent ZPGFPBL to document the variations in pressure gradient with streamwise distance inside and outside the boundary layer. Figure 6 presents the mean wall static pressure gradient $C_{pw} = (p_{y=0,x} - p_{y=0,x=0})/(\frac{1}{2}\rho U_\infty^2)$, and two other mean streamwise pressure gradient parameters, β and P^+. It is impractical in either experiments or DNS to achieve a strictly zero streamwise pressure gradient. For example in the work of Adrian *et al.* (2000) streamwise pressure gradient was made to vanish to within 0.2 %–3.8 % of the free stream dynamic pressure over a test-section length of approximately 80δ, by adjusting the contour of the test-section ceiling, depending upon Reynolds number.

The issue that arises naturally is how to judge the smallness of the streamwise pressure gradient. Here, we quantify the deviation of our streamwise pressure gradient from nominally zero by comparing our parameters with those used by Spalart & Watmuff (1993) in their study of an attached flat-plate turbulent boundary layer under moderate levels of imposed favourable and adverse streamwise pressure gradients. In the boundary layer of Spalart & Watmuff (1993), C_{pw} varies between -0.45 and 0.1 over a streamwise range of $500 < Re_\theta < 1600$. In our boundary layer C_{pw} is bracketed by 0 and 0.012 over the streamwise range of $80 < Re_\theta < 940$. Near the exit the convective outflow boundary condition causes rather a rapid descent in our C_{pw}. The β parameter of Spalart & Watmuff varies from -0.3 to $+2$; this is contrasted with our much narrower variation range for β from -0.03 to 0.01. In the flow of Spalart & Watmuff, $-0.009 < P^+ < 0.02$; in our flow, $-0.0007 < P^+ < 0.0005$. It is quite clear

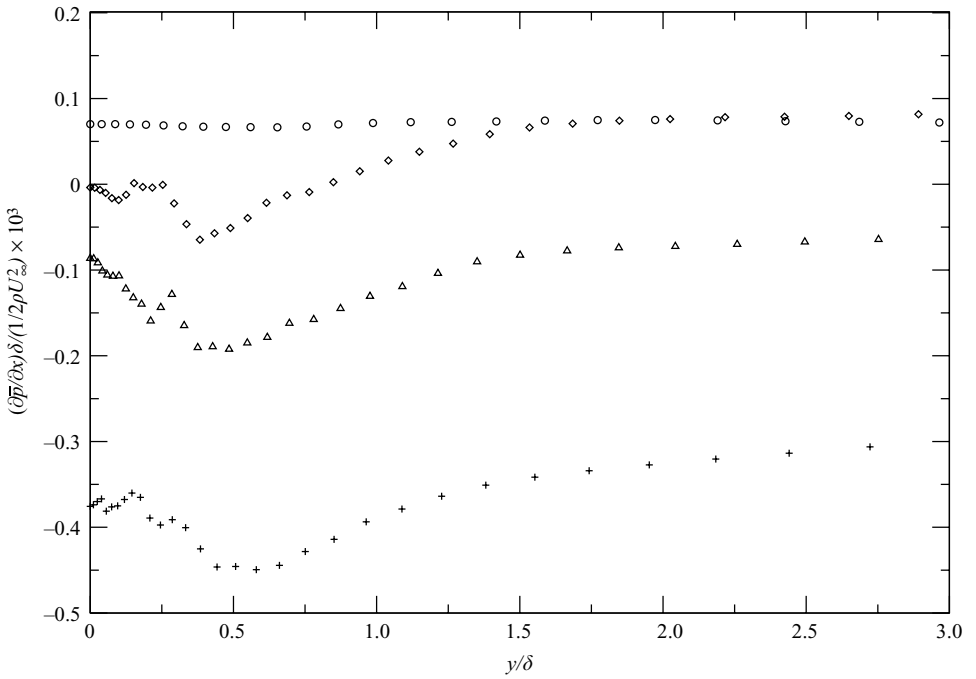

FIGURE 7. Mean streamwise pressure gradient $(\partial\overline{p}/\partial x)\delta/(1/2\rho U_\infty^2) \times 10^3$ as a function of y/δ. Circle, $Re_\theta = 200$; diamond, $Re_\theta = 400$; triangle, $Re_\theta = 600$; plus, $Re_\theta = 800$.

that the streamwise pressure gradient in our flow is approximately 1–2 orders of magnitude weaker, depending upon location, than in the flow of Spalart & Watmuff (1993). The streamwise pressure gradient as a function of the wall-normal distance is presented in figure 7 for four different momentum thickness Reynolds numbers. Contrary to the classical boundary layer assumption, the wall-normal variation of the pressure gradient is not negligible within the boundary layer in the post-transition regime.

Skin-friction coefficient C_f is shown in figure 8. At about $Re_\theta = 750$ the slope of C_f turns to mildly negative, indicating that the transition process may have been completed. In the turbulent region, C_f agrees with the experimental data of Murlis, Tsai & Bradshaw (1982) and Adrian *et al.* (2000). It is interesting that instantaneous skin friction in the turbulent region displays extremely large fluctuations (which may be related to the regular passage of isotropic turbulence slabs). The minimum instantaneous value at this particular instant almost reaches zero, and peak values are four to five times larger than the mean. Figure 9 shows the turbulent skin-friction intensity, $\tau_{w,rms}^{'+}$, and wall-pressure intensity distributions. The r.m.s. level of the wall shear stress fluctuations in the turbulent region is in good agreement with the 40 % of the mean value measured by Alfredsson *et al.* (1988), notwithstanding the difference in the Reynolds number. The data of Kim *et al.* (1987) show that $\tau_{w,rms}^{'+} = 36\,\%$ of the mean skin friction in their channel flow. In this figure, the wall-pressure fluctuations are normalized by the mean wall shear stress. The sharp drop and rise of $p_{w,rms}^{'+}$ at the inlet and outlet are related to the imposed boundary conditions. Our $p_{w,rms}^{'+}$ in the turbulent region is somewhat lower than the value of Spalart (1988) (see figure 26), but still within the general range of the experimental data reviewed by Willmarth (1975).

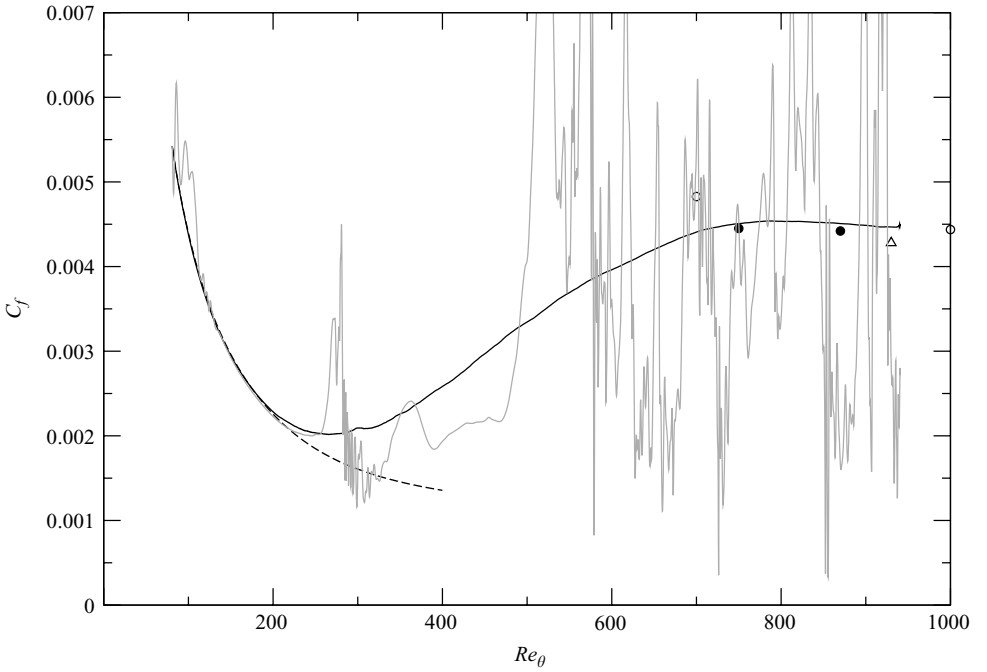

FIGURE 8. Mean skin-friction coefficient C_f as a function of momentum thickness Reynolds number Re_θ. Solid line, present DNS; dashed line, Blasius solution; solid circle, Murlis *et al.* (1982); open circle, Purtell *et al.* (1981); triangle, Adrian *et al.* (2000). Light solid line, instantaneous skin-friction coefficient along the x-axis at an arbitrary z at $t = 100.1\mathscr{T}$.

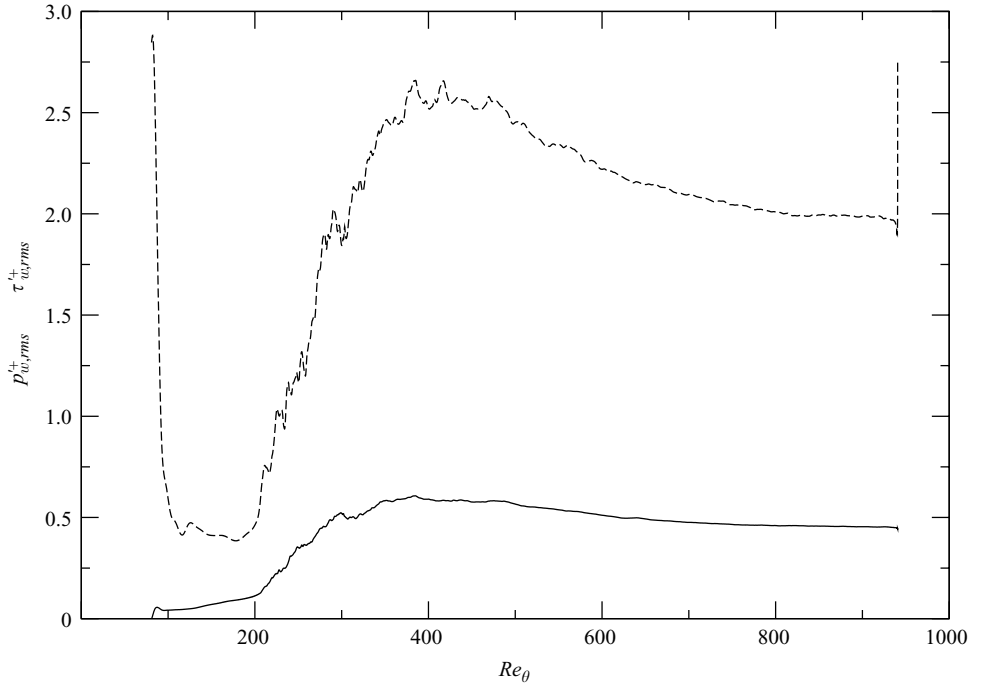

FIGURE 9. Variations of wall pressure fluctuation $p'^{+}_{w,rms}$ (dashed line) and wall shear stress fluctuation $\tau'^{+}_{w,rms}$ (solid line) with Re_θ.

The mean skin-friction coefficient C_f follows the Blasius solution to within 1 % until $Re_\theta = 180$, which is presumably the average laminar breakdown station. Apparently the imposed moderate levels of free stream disturbances do not alter the Blasius layer in the early transitional region. The importance of maintaining the Blasius layer prior to breakdown was recognized early by Schubauer & Skramstad (1947). If the imposed disturbances are sufficiently large so that the base flow is substantially modified, there would be no early transitional region in which linear stability theory would apply. In that case one cannot distinguish the base flow from the perturbed flow since the base flow itself has also been distorted. Therefore, even in bypass transition investigations, it is still important to properly control the disturbance level if one intends to apply linear theory to the early transitional region.

Previous studies have shown that a turbulent boundary layer can be maintained for Re_θ as low as 225–300. However, the converse statement is not true; $Re_\theta = 300$ will not guarantee a ZPGFPBL to be turbulent. For example, the present boundary layer remains transitional until approximately $Re_\theta = 750$. At the inlet ($Re_\theta = 80$), figure 8 shows that the introduced isotropic turbulence slab produces only a moderate level of instantaneous skin-friction deviation away from the Blasius value. But outside the location range of the slab, the instantaneous skin-friction follows the Blasius profile in the early transitional region. Overall, all these global parameters indicate that under the prescribed flow design, the present boundary layer breakdown occurs on average at $Re_\theta = 180$ and transition is complete by $Re_\theta = 750$.

3.3. *Statistics in the turbulent region*

3.3.1. *Mean velocity*

Statistics of the computed boundary layer at one turbulent station, $Re_\theta = 900$, are presented in detail in this section. The boundary layer thickness normalized by the inner wall coordinate is $\delta^+ = 400$. Mean velocity $\overline{u}/U_\infty$ as a function of the outer wall-normal coordinate y/δ^* is compared with the experimental data of Purtell, Klebanoff & Buckley (1981) at $Re_\theta = 1000$ in figure 10.

Figure 11 shows the computed mean-velocity profile $\overline{u}^+$ plotted in semi-logarithmic form. There is good agreement with the linear profile below $y^+ = 4$, and with the experimental data of Murlis *et al.* (1982) at $Re_\theta = 791$ for $y^+ > 40$. The agreement is interesting considering the fact that the present $\overline{u}^+$ is obtained by scaling the mean velocity with a directly computed wall shear stress, and the experimental $\overline{u}^+$ was obtained by scaling the mean velocity with a wall shear stress from a best fit to an assumed log law. Our $\overline{u}^+$ also agrees well with the DNS of Spalart (1988) at $Re_\theta = 670$ except in the wake region.

Figure 12 shows mean velocity deficit $(U_\infty - \overline{u})/u_\tau$ as a function of y/δ together with the experimental data of Erm, Smits & Joubert (1985), Smith (1994) and DeGraaff & Eaton (2000) over a wide range of $617 < Re_\theta < 4980$. Quite clearly, the universal velocity defect scaling law does not apply for these data. The modified scaling of $(U_\infty - \overline{u})\delta/(U_\infty \delta^*)$ proposed by Zagarola & Smits (1998) yields a slightly better collapse across certain regions and is also shown in the figure. Profiles of $\mathrm{d}\overline{u}^+/\mathrm{dln}y^+$ and $\mathrm{dln}\overline{u}^+/\mathrm{dln}y^+$ are shown in figure 13. Our results show good agreement with those from Spalart (1988) and with the composite curve of Monkewitz *et al.* (2007). These two sets of low-Reynolds-number DNS also display nearly identical trends as those of Smith's high-Reynolds-number experimental data for the mean velocity gradients. The trends of the mean velocity gradient profiles presented in figure 13 are also qualitatively similar to those discussed in detail by Wu & Moin (2008) in a DNS study on the turbulent pipe flow.

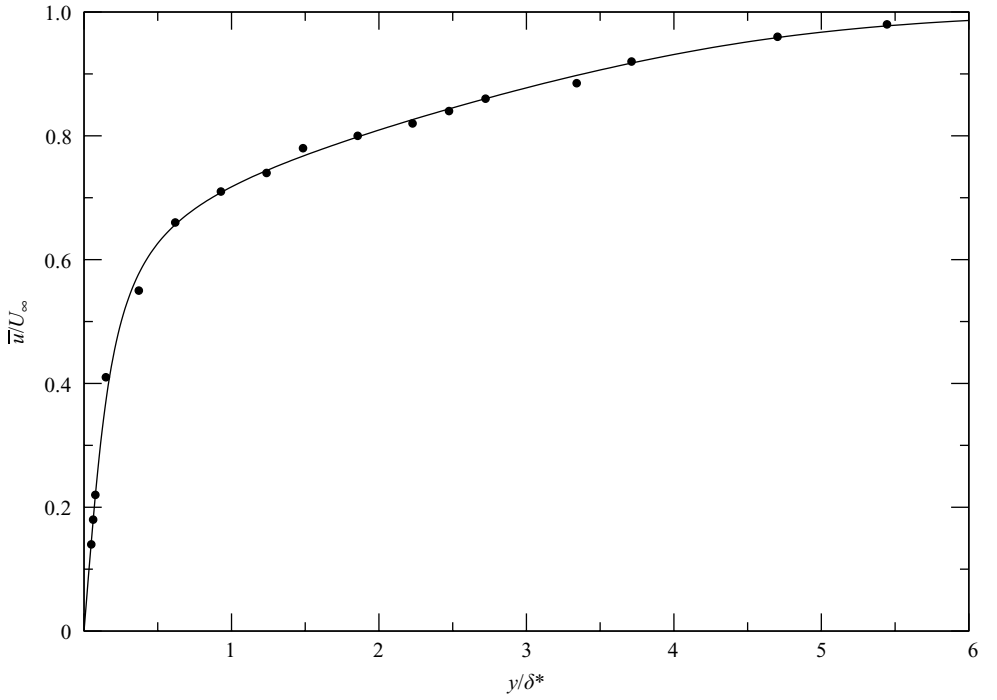

FIGURE 10. Normalized mean velocity profile $\overline{u}/U_\infty$ as a function of outer coordinate y/δ^* in the turbulent region. Solid line, present DNS at $Re_\theta = 900$; circle, Purtell *et al.* (1981) at $Re_\theta = 1000$.

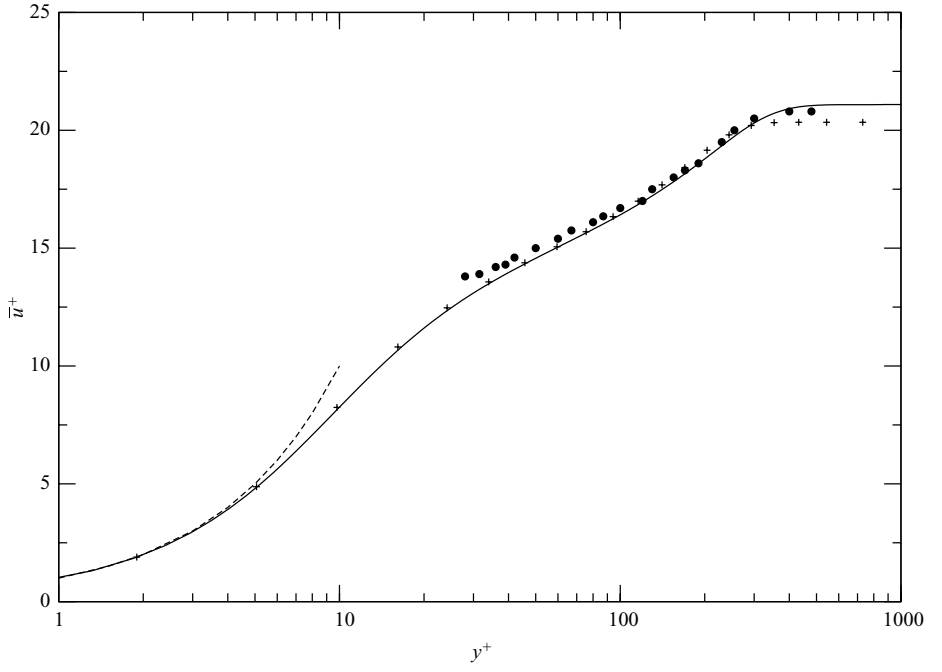

FIGURE 11. Mean velocity profile $\overline{u}^+$ as a function of y^+ in the turbulent region. Solid line, present DNS at $Re_\theta = 900$; dashed line, $\overline{u}^+ = y^+$; solid circle, Murlis *et al.* (1982) at $Re_\theta = 791$; plus, Spalart (1988) at $Re_\theta = 670$.

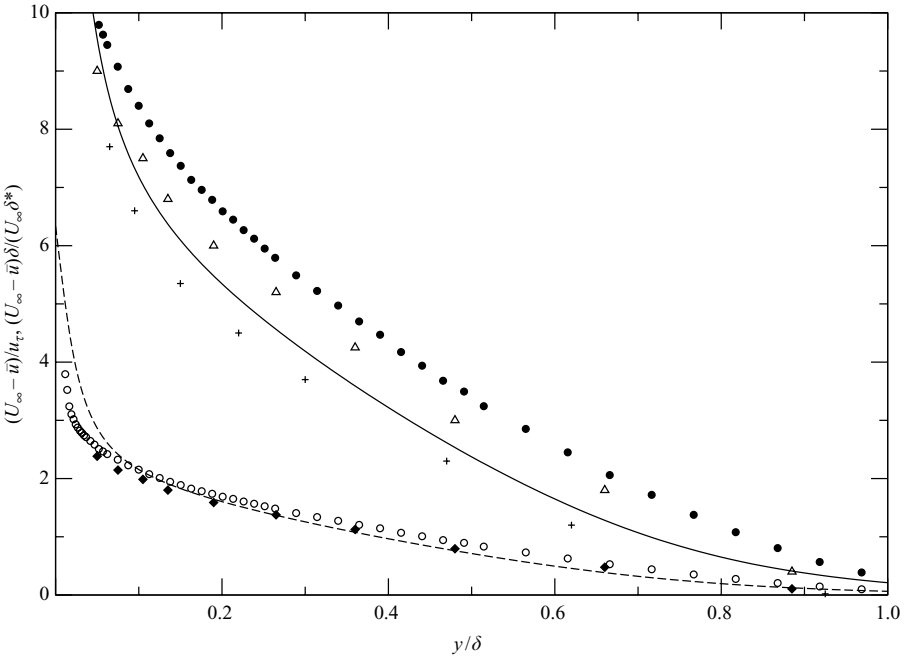

FIGURE 12. Mean velocity defect profiles as a function of outer coordinate y/δ in the turbulent region. Present DNS at $Re_\theta = 900$: solid line, $(U_\infty - \overline{u})/u_\tau$; dashed line, $(U_\infty - \overline{u})\delta/(U_\infty\delta^*)$. Smith (1994) at $Re_\theta = 4980$: solid circle, $(U_\infty - \overline{u})/u_\tau$; open circle, $(U_\infty - \overline{u})\delta/(U_\infty\delta^*)$. DeGraaff & Eaton (2000) at $Re_\theta = 1430$: triangle, $(U_\infty - \overline{u})/u_\tau$; diamond, $(U_\infty - \overline{u})\delta/(U_\infty\delta^*)$. Erm *et al.* (1985) at $Re_\theta = 617$: plus, $(U_\infty - \overline{u})/u_\tau$.

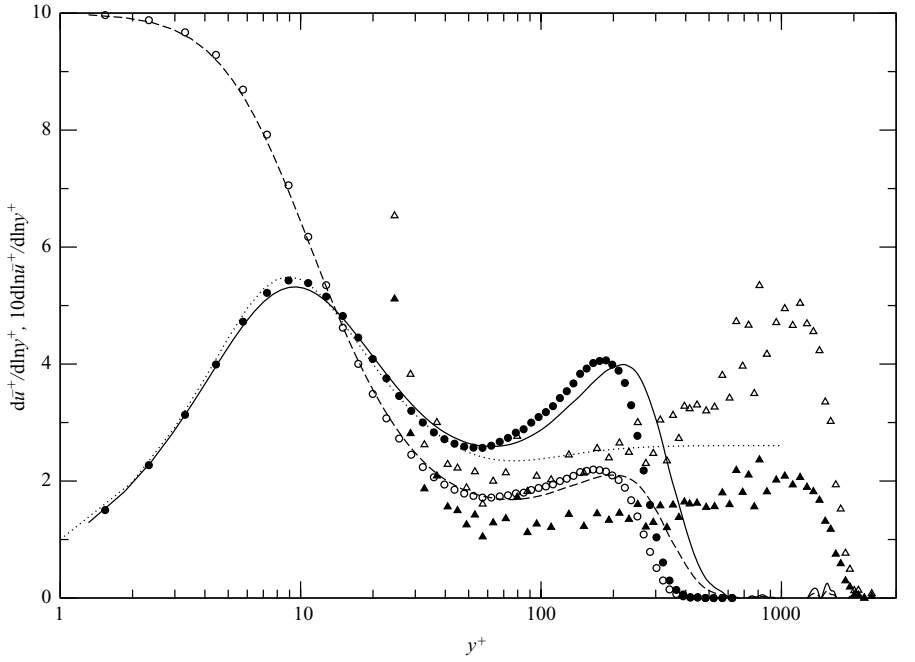

FIGURE 13. Mean velocity gradients as a function of inner wall coordinate y^+ in the turbulent region. Present DNS at $Re_\theta = 900$: solid line, $d\overline{u}^+/d\ln y^+$; dashed line, $10d\ln\overline{u}^+/d\ln y^+$. Circle, Spalart (1988) at $Re_\theta = 670$; triangle, Smith (1994) at $Re_\theta = 4980$; dotted line, Monkewitz *et al.* (2007).

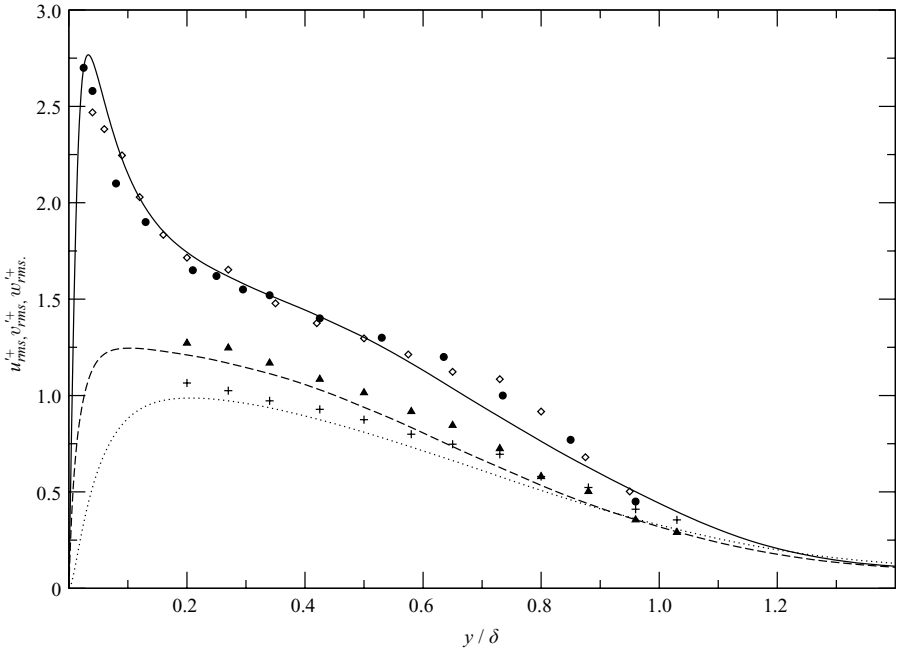

FIGURE 14. Turbulence intensities as a function of outer coordinate y/δ in the turbulent region. Lines are from the present DNS at $Re_\theta = 900$. Solid line, u'^{+}_{rms}; dotted line, v'^{+}_{rms}; dashed line, w'^{+}_{rms}; solid circle, Purtell *et al.* (1981) at $Re_\theta = 1340$; all other symbols, Erm & Joubert (1991) at $Re_\theta = 697$.

3.3.2. *Second-order statistics*

Honkan & Andreopoulos (1997) compared the profiles of Reynolds stresses from 11 groups. Their study showed that the differences are substantial especially near the wall. In particular, they observed that existing experimental data of the Reynolds shear stress in the near wall region for a ZPGFPBL show no consistent trends and do not agree with the DNS of Spalart, as indicated by their figure 11(*c*). Over a narrow Reynolds number range of $2600 < Re_\theta < 2790$ the peak streamwise intensities differ by more than 20 %, and the difference in the wall-normal intensity is over 50 %. Honkan and Andreopoulos attributed these discrepancies to spatial resolution effects of the probes, differences in the measurement techniques and the errors involved in controlling the experimental conditions. They also commented that the classical data from Klebanoff may be contaminated by the upstream long roughness strip used to trip the boundary layer.

Figures 14 and 15 show the normalized turbulence intensities at $Re_\theta = 900$ in outer and inner wall units, respectively. Also shown in the figures are the data of Erm & Joubert (1991) as well as the streamwise turbulence intensity u'^{+}_{rms} from Purtell *et al.* (1981) at $Re_\theta = 1340$. Purtell *et al.* did not measure the other two turbulence intensity components. Spalart's data are also included in figure 15. The agreement of u'^{+}_{rms} between the present DNS and low-Reynolds-number experimental data is satisfactory. The peak of u'^{+}_{rms} is 2.77 located at approximately $y^+ = 13$. A plateau in the wall-normal turbulence intensity $v'^{+}_{rms} \approx 0.95$ spans from $y^+ = 60$ to 100. The peak of v'^{+}_{rms} is located at approximately 0.2δ or 80 inner wall units. The survey done by Honkan & Andreopoulos (1997) shows that the plateau value in v'^{+}_{rms} varies

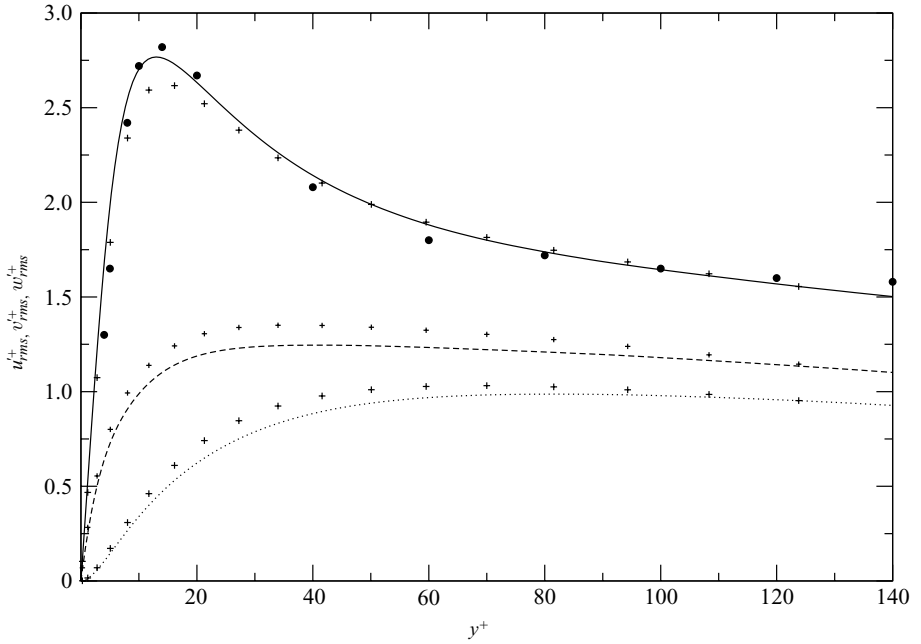

FIGURE 15. Turbulence intensities as a function of inner wall coordinate y^+ in the turbulent region. Lines are from the present DNS at $Re_\theta = 900$. Solid line, u'^+_{rms}; dotted line, v'^+_{rms}; dashed line, w'^+_{rms}; solid circle, Purtell *et al.* (1981) at $Re_\theta = 1340$; plus, Spalart (1988) at $Re_\theta = 670$.

over a substantial range from 0.8 to 1.4 as reported by different groups for various Reynolds numbers. The current value of 0.95 is close to that from Spalart. Spanwise turbulence intensity w'^+_{rms} also exhibits a plateau of 1.25 spanning from $y^+ = 20$ to 60, approximately. The experimental data of Honkan & Andreopoulos (1997) in their figure 14 displays a very near-wall peak in w'^+_{rms} at $y \approx 0.02\delta$. This is either due to their somewhat higher Reynolds number or experimental errors. Outside the boundary layer, it is seen from figure 14 that in the current boundary layer at $Re_\theta = 900$ the three turbulence intensities nearly collapse, indicating an approach to isotropy just outside the boundary layer.

From the time of $t = 60\mathscr{T}$ to $t = 100\mathscr{T}$, velocity signals were saved at an array of preselected locations for the purpose of frequency spectra computation. All the recorded points are located in the $z = 187.5$ plane. The procedure for computation of the frequency power spectrum follows the one discussed in Choi & Moin (1990). The $N = 80\,000$ time samples were divided into overlapping segments, each containing 1024 points. Figure 16 shows the spectra of streamwise velocity fluctuations at four y-locations inside the boundary layer in the turbulent region at $Re_\theta = 915$ ($x = 6094\theta_0$). The first y-location of 0.0133δ is equivalent to $y^+ = 5.27$. At this location, $\overline{u'^2}$ has relatively low energy levels in the intermediate frequency range of $100 < \omega\delta/u_\tau < 1000$. The spectra exhibit an approximate -1 slope in the low-frequency region of $30 < \omega\delta/u_\tau < 90$, similar to the -1 slope reported from the pipe flow measurements of Perry, Henbest & Chong (1986). Turan, Azad & Kassab (1987) reported that in turbulent ZPGFPBL, the logarithmic law of mean velocity and the k_x^{-1} spectral law appear to exist at the same wall-normal position simultaneously. The spectra of streamwise velocity fluctuations do not yield a significant range with $-5/3$ slope in the intermediate frequency range (most likely due to the low Reynolds

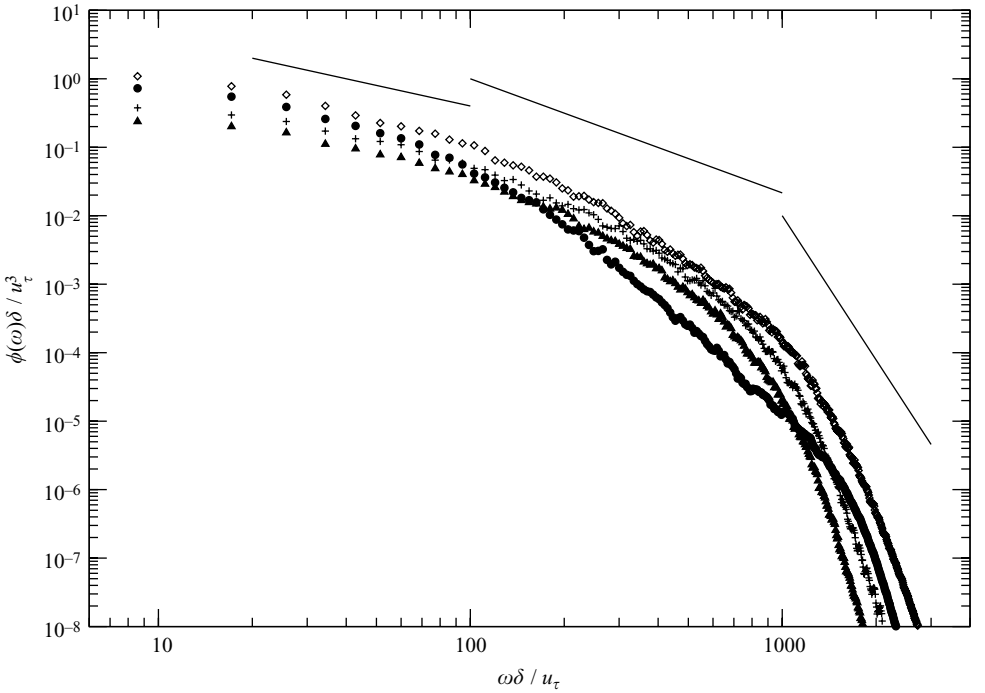

FIGURE 16. Frequency spectra of streamwise velocity fluctuations in the turbulent region at $Re_\theta = 915$. Solid circle, $y = 0.0133\delta$ ($y^+ = 5.27$); diamond, $y = 0.0667\delta$ ($y^+ = 26.43$); plus, $y = 0.267\delta$; triangle, $y = 0.533\delta$. Solid lines from left to right, -1 slope, $-5/3$ slope and -7 slope, respectively.

number of the DNS). Spectra of the wall-normal velocity fluctuations at the same spatial locations are presented in figure 17. In the low frequency range of $\omega\delta/u_\tau < 100$ the spectra are relatively flat in the current logarithmic scale. Compared to the results for $\overline{u'^2}$ the well-known $-5/3$ slope can now be more easily discerned from the $\overline{v'^2}$ spectra in the intermediate frequency range of $200 < \omega\delta/u_\tau < 400$.

Shear stresses at $Re_\theta = 900$ are presented in figures 18 and 19 using outer and inner wall units, respectively. Also shown in the figures are the Reynolds shear stress results from Spalart (1988), Honkan & Andreopoulos (1997) and DeGraaff & Eaton (2000). The most notable feature from these two figures is the overshoot in the total shear stress $\tau^+ = -\overline{u'v'}^+ + (\nu \mathrm{d}\overline{u}/\mathrm{d}y)^+$ in the region $y^+ < 20$. The normal gradient is still zero at the wall. This feature will be discussed in more detail in the next subsection. The prevailing view, and a basis for turbulence theories in the wall layer, is that in a ZPGFPBL the maximum total shear stress is attained at the wall, and the wall-normal variation of τ is a monotonic decrease from the wall to the boundary layer edge. Our results in figures 18 and 19 do not support this notion.

Budget terms in the mean streamwise momentum transport equation are shown in figure 20 for the near-wall region at $Re_\theta = 900$. Except for the gradients of viscous and Reynolds shear stress terms, all other terms are multiplied by a factor of 100 to display their dependency on y^+. Clearly the dominant terms are the wall-normal derivatives of the shear stresses which balance each other. The balance term shows that the calculation has reached a statistically steady state.

The good agreement between our boundary layer statistics with classic ZPGFPBL experimental data in the turbulent region downstream of $Re_\theta = 750$ suggests that they

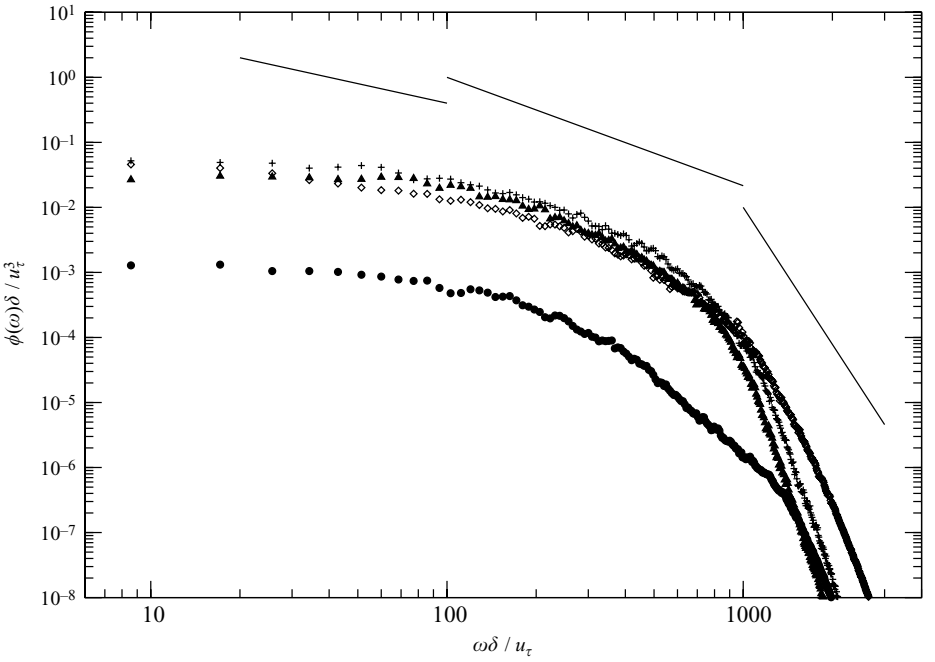

FIGURE 17. Frequency spectra of wall-normal velocity fluctuations in the turbulent region at $Re_\theta = 915$. Solid circle, $y = 0.0133\delta$ ($y^+ = 5.27$); diamond, $y = 0.0667\delta$; plus, $y = 0.267\delta$; triangle, $y = 0.533\delta$. Solid lines from left to right, -1 slope, $-5/3$ slope and -7 slope, respectively.

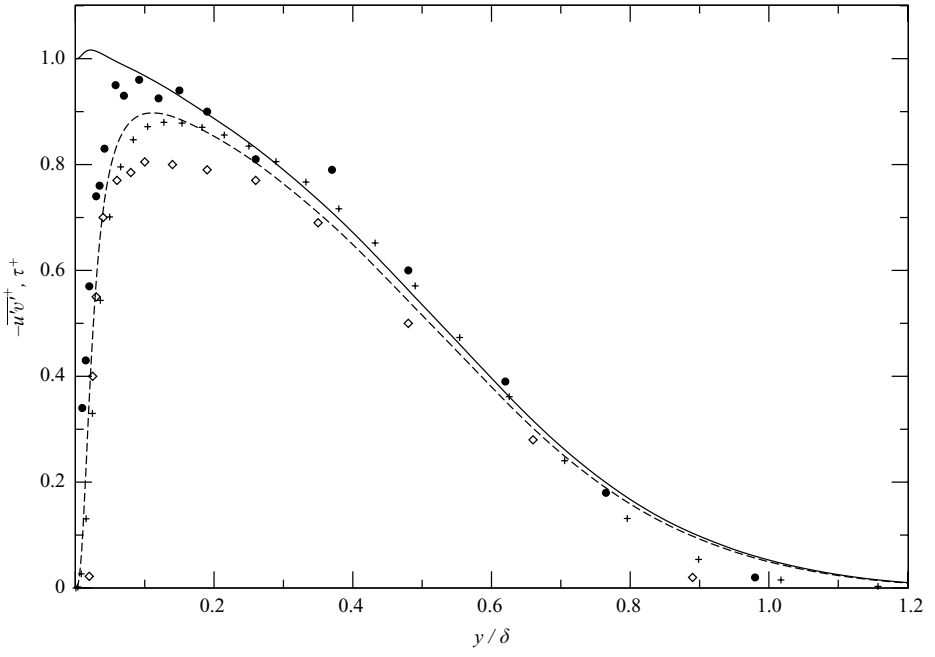

FIGURE 18. Reynolds and total shear stresses as a function of outer coordinate y/δ. Solid line, τ^+ from present DNS at $Re_\theta = 900$; dashed line, $-\overline{u'v'}^+$ from present DNS at $Re_\theta = 900$; solid circle, Honkan & Andreopoulos (1997) at $Re_\theta = 2790$; diamond, DeGraaff & Eaton (2000) at $Re_\theta = 1430$; plus, Spalart (1988) at $Re_\theta = 670$.

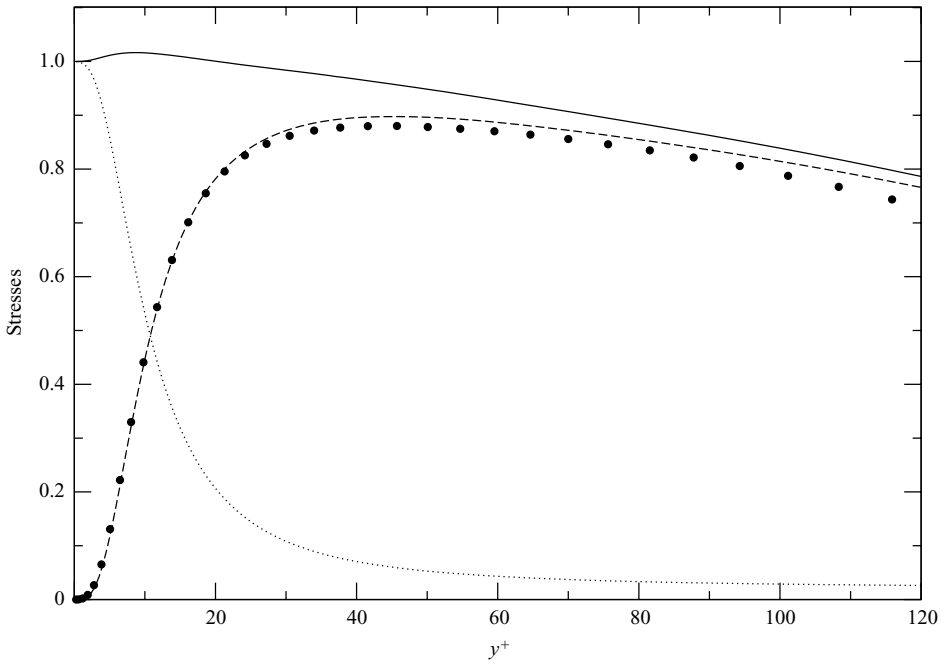

FIGURE 19. Reynolds, viscous and total shear stresses as a function of inner wall coordinate y^+. Lines: present DNS at $Re_\theta = 900$; solid line, τ^+; dashed line, $-\overline{u'v'}^+$; dotted line, viscous shear stress $(\nu \mathrm{d}\overline{u}/\mathrm{d}y)^+$; solid circle, Reynolds shear stress from Spalart (1988) at $Re_\theta = 670$.

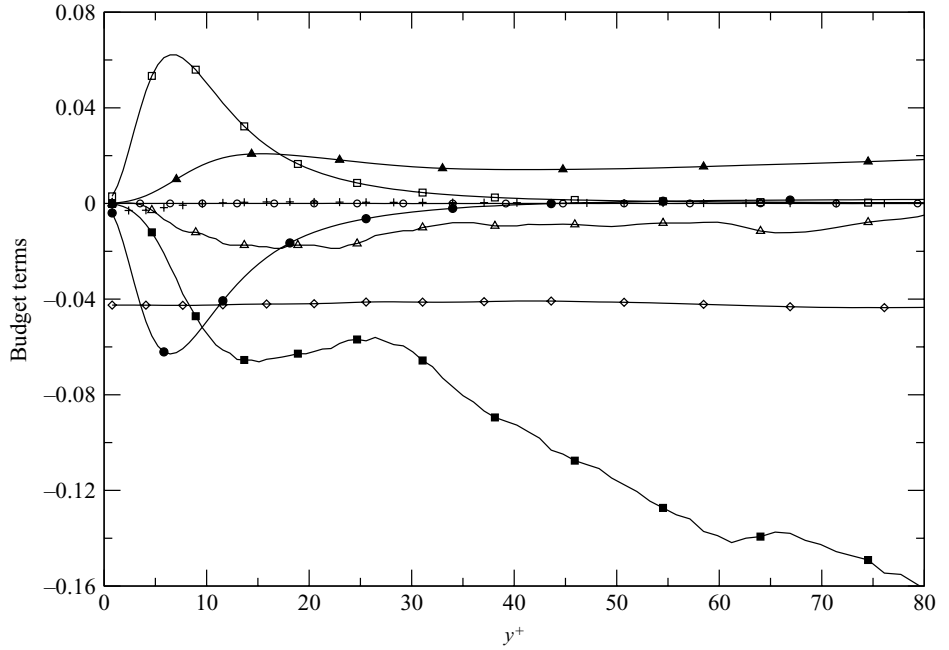

FIGURE 20. Budget terms in mean streamwise momentum equation as a function of inner wall coordinate y^+ at $Re_\theta = 900$. Open circle, $-100\nu(\partial^2\overline{u}/\partial x^2)$; open box, $-\nu(\partial^2\overline{u}/\partial y^2)$; open diamond, $(100/\rho)(\partial\overline{p}/\partial x)$; open triangle, $100\partial\overline{u'^2}/\partial x$; solid circle, $\partial\overline{u'v'}/\partial y$; solid box, $100\overline{u}(\partial\overline{u}/\partial x)$; solid triangle, $100\overline{v}(\partial\overline{u}/\partial y)$; plus, balance of budgets. All budget terms are normalized by U_∞^2/δ.

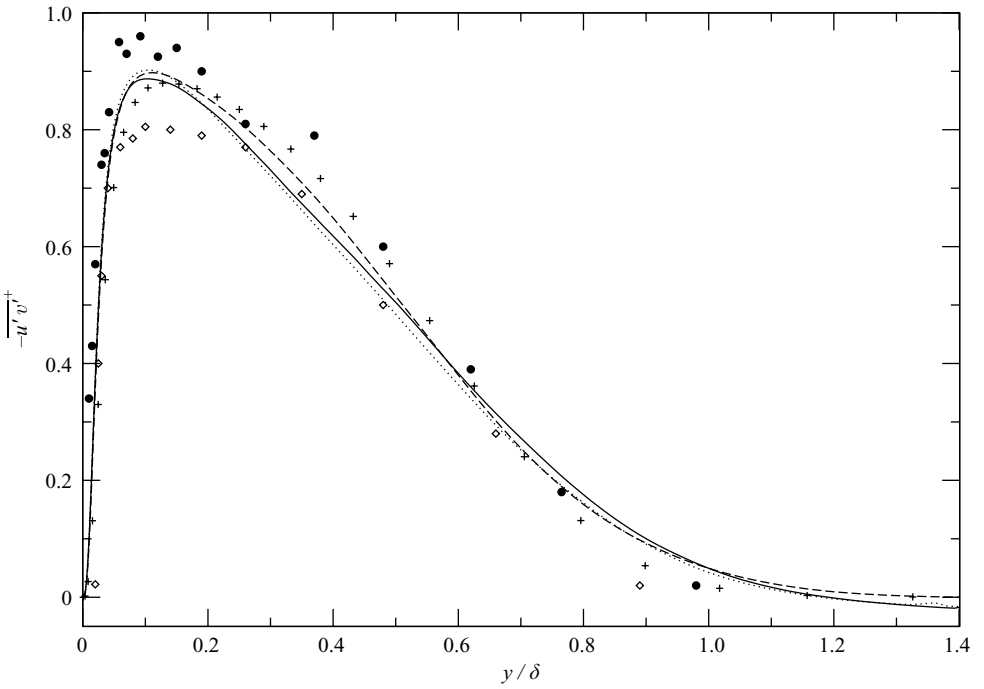

FIGURE 21. Assessment of the free stream disturbance effect on boundary layer statistics using Reynolds shear stress at $Re_\theta = 900$. Solid line, free stream disturbance from passing wakes constrained to be 6δ away from the wall at the inlet; dotted line, free stream disturbance from unconstrained passing wakes; dashed line, present simulation; circle, Honkan & Andreopoulos (1997) at $Re_\theta = 2790$; diamond, DeGraaff & Eaton (2000) at $Re_\theta = 1430$; plus, Spalart (1988) at $Re_\theta = 670$.

bear negligible signatures of the decaying free stream turbulent slab. This point is further demonstrated by figure 21 which compares the present Reynolds shear stress profile at $Re_\theta = 900$ with those obtained from two additional DNS calculations of a different ZPGFPBL under the perturbation of free stream passing wakes using a procedure similar to that of Wu *et al.* (1999).

3.4. *Statistics in the late transitional region*

The present boundary layer undergoes a well-controlled transition process. The streamwise pressure gradient is nominally zero, and the imposed perturbations inside the boundary layer are weak. This makes it possible to divide the entire process into early and late transitional stages. The early transitional region is a Blasius layer under weak perturbations in which statistical measures such as integral parameters as well as local velocity profiles deviate only slightly from their theoretical values (see figures 8). Both the skin-friction coefficient C_f and the shape factor H are excellent indicators for identifying the late transitional stage. Structurally, the late transitional region is marked by the onset of turbulent spot from the low end, i.e. breakdown of the Blasius layer.

The statistics at six streamwise stations from $Re_\theta = 200$ to 800 are documented, although the last station may also be considered as turbulent. Mean velocity profiles are shown in figure 22; turbulence intensities and pressure fluctuations are presented in figure 23–26, and Reynolds shear stress is presented in figure 27. Spalart's DNS statistics at $Re_\theta = 670$ are added in all these figures to serve as a reference indicator

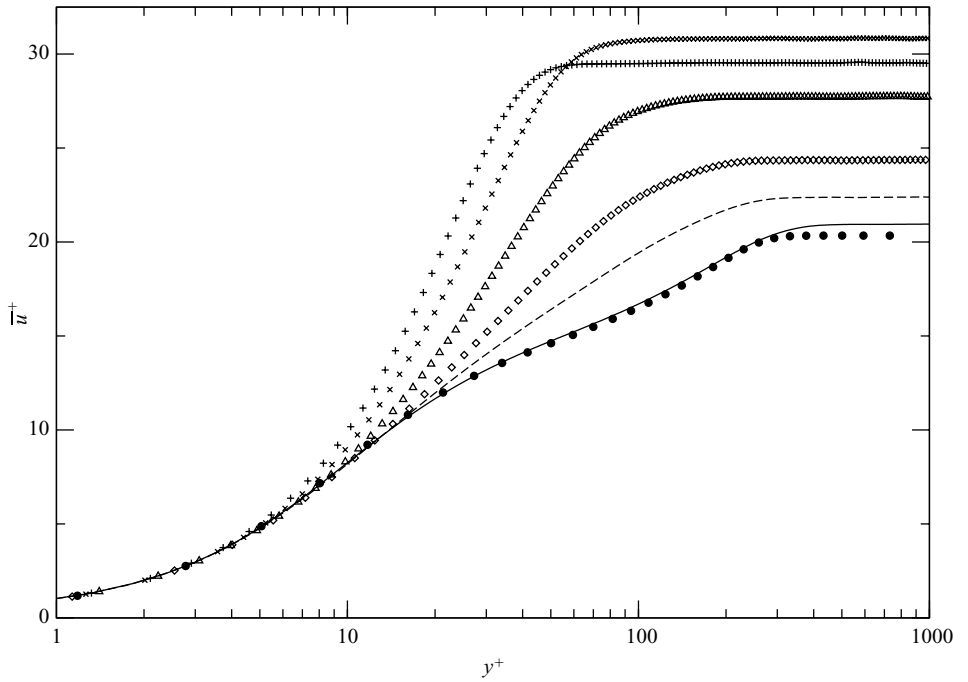

FIGURE 22. Mean velocity profile $\overline{u}^+$ as a function of inner wall coordinate y^+ in the late transitional region. Plus, $Re_\theta = 200$; cross, $Re_\theta = 300$; triangle, $Re_\theta = 400$; diamond, $Re_\theta = 500$; dashed line, $Re_\theta = 600$; solid line, $Re_\theta = 800$; circle, Spalart (1988) at $Re_\theta = 670$.

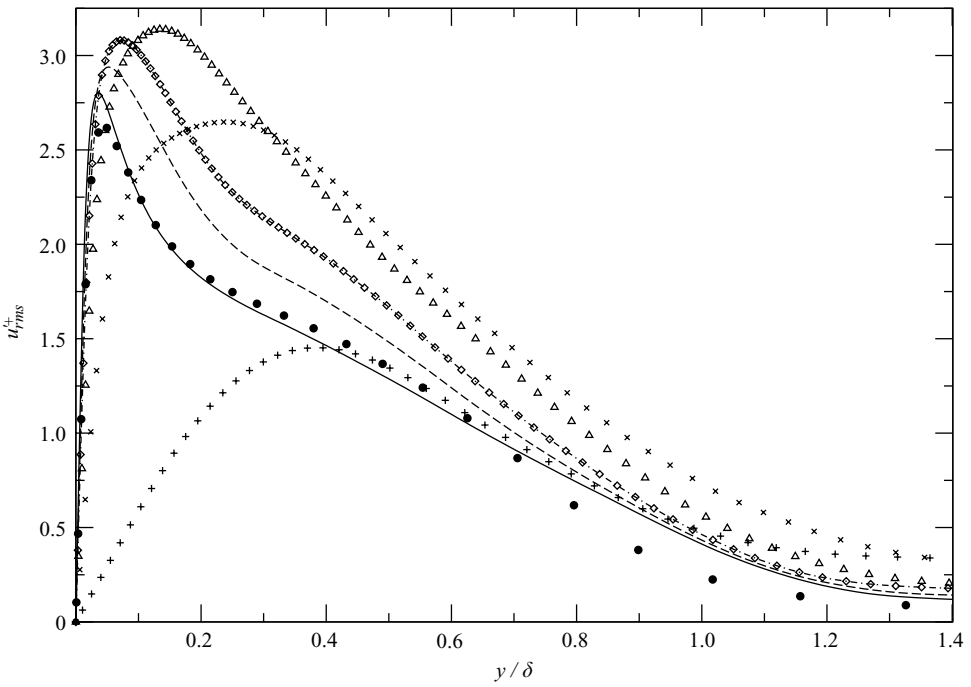

FIGURE 23. u'^+_{rms} as a function of outer coordinate y/δ in the late transitional region. Plus, $Re_\theta = 200$; cross, $Re_\theta = 300$; triangle, $Re_\theta = 400$; diamond, $Re_\theta = 500$; dashed line, $Re_\theta = 600$; solid line, $Re_\theta = 800$; circle, Spalart (1988) at $Re_\theta = 670$.

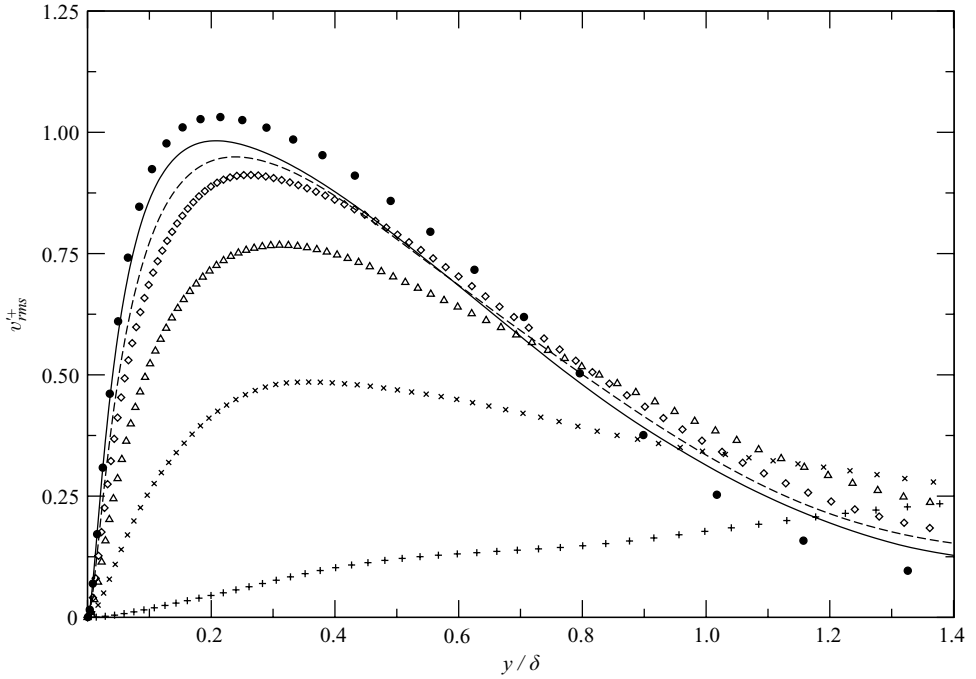

FIGURE 24. v'^{+}_{rms} as a function of outer coordinate y/δ in the late transitional region. Plus, $Re_\theta = 200$; cross, $Re_\theta = 300$; triangle, $Re_\theta = 400$; diamond, $Re_\theta = 500$; dashed line, $Re_\theta = 600$; solid line, $Re_\theta = 800$; circle, Spalart (1988) at $Re_\theta = 670$.

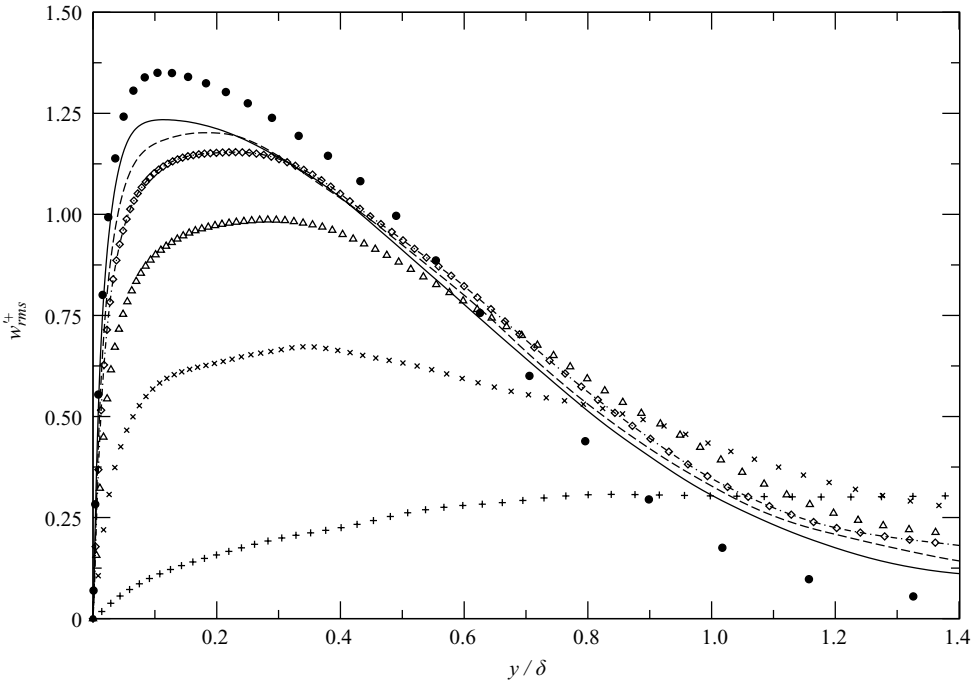

FIGURE 25. w'^{+}_{rms} as a function of outer coordinate y/δ in the late transitional region. Plus, $Re_\theta = 200$; cross, $Re_\theta = 300$; triangle, $Re_\theta = 400$; diamond, $Re_\theta = 500$; dashed line, $Re_\theta = 600$; solid line, $Re_\theta = 800$; circle, Spalart (1988) at $Re_\theta = 670$.

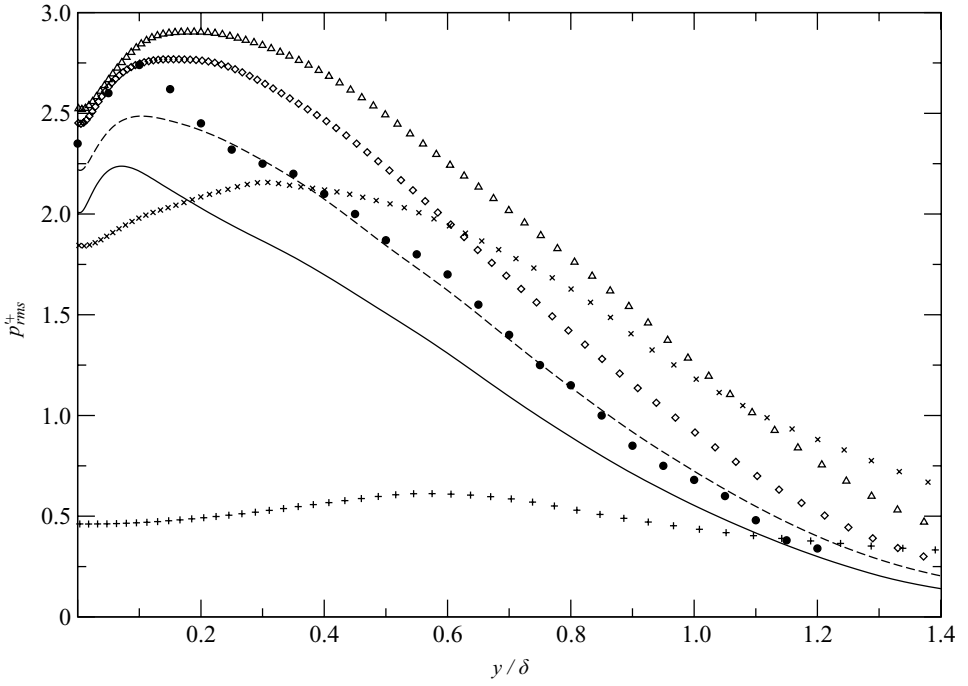

FIGURE 26. p'^{+}_{rms} as a function of outer coordinate y/δ in the late transitional region. Plus, $Re_\theta = 200$; cross, $Re_\theta = 300$; triangle, $Re_\theta = 400$; diamond, $Re_\theta = 500$; dashed line, $Re_\theta = 600$; solid line, $Re_\theta = 800$; circle, Spalart (1988) at $Re_\theta = 670$.

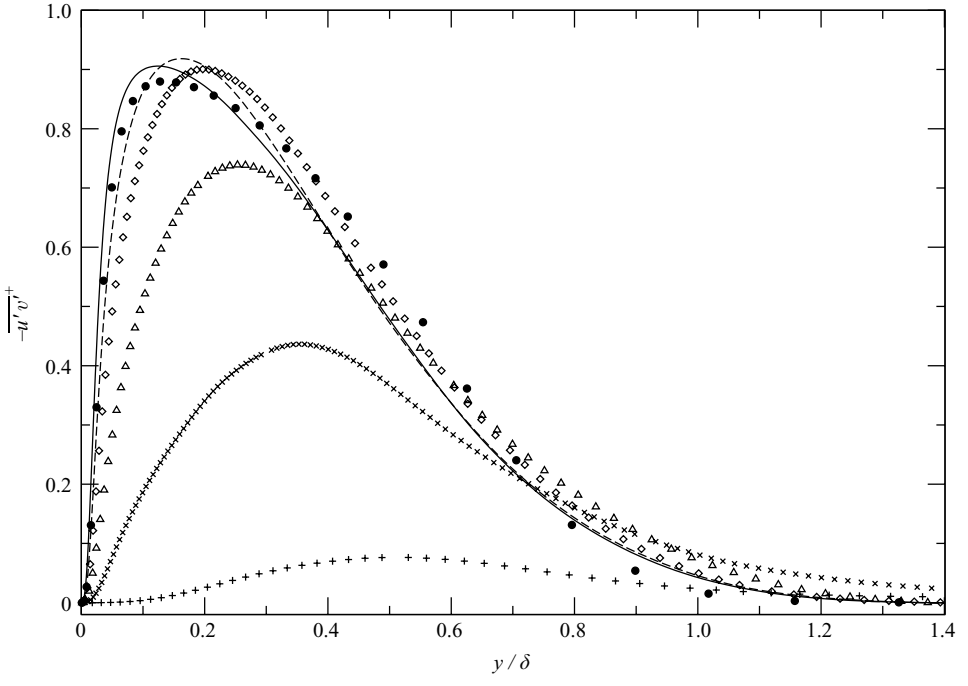

FIGURE 27. $-\overline{u'v'}^{+}$ as a function of outer coordinate y/δ in the late transitional region. Plus, $Re_\theta = 200$; cross, $Re_\theta = 300$; triangle, $Re_\theta = 400$; diamond, $Re_\theta = 500$; dashed line, $Re_\theta = 600$; solid line, $Re_\theta = 800$; circle, Spalart (1988) at $Re_\theta = 670$.

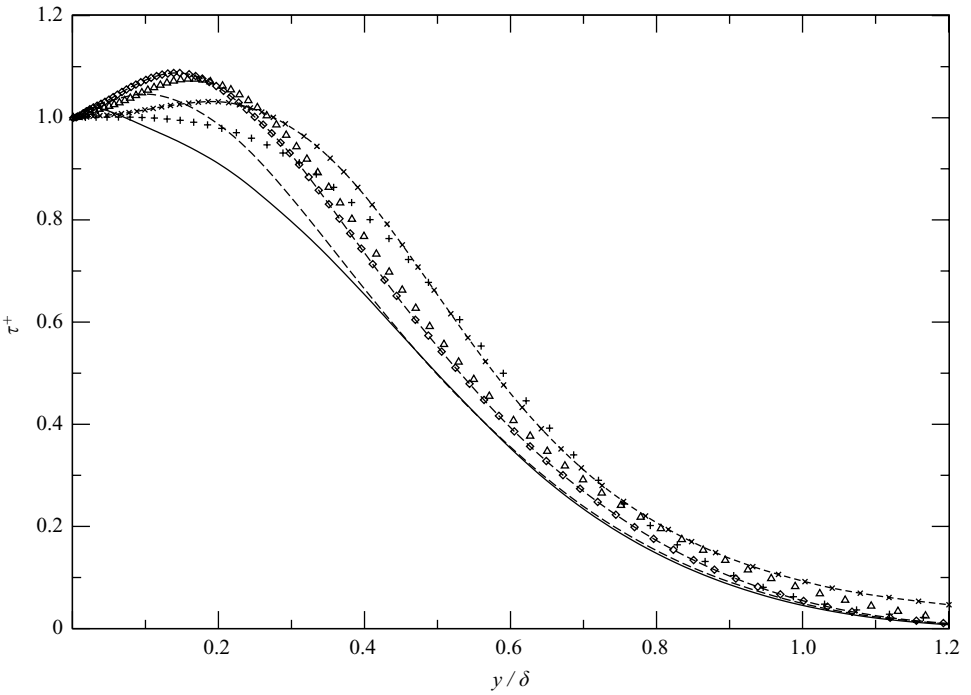

FIGURE 28. τ^+ as a function of outer coordinate y/δ in the late transitional region. Plus, $Re_\theta = 200$; cross, $Re_\theta = 300$; triangle, $Re_\theta = 400$; diamond, $Re_\theta = 500$; dashed line without symbol, $Re_\theta = 600$; solid line, $Re_\theta = 800$.

of turbulent state. Note that our boundary layer thickness δ is based on the well-accepted definition of 99 % of U_∞, but Spalart's δ was constructed differently. These figures show that when plotted against y/δ, the peak locations of all three turbulence intensities, pressure fluctuation and the Reynolds shear stress shift monotonically towards the wall with an increase in the streamwise distance x or equivalently Re_θ. The fact that v'^+_{rms} at $Re_\theta = 200$ is still increasing with y at $y/\delta = 1.2$ indicates that the length scale of the free stream turbulence is somewhat larger than the local δ.

Figure 28 shows the variation of the total shear stress with outer coordinate y/δ at six streamwise stations from $Re_\theta = 200$ to 800. Starting from no overshoot in the Blasius layer at $Re_\theta = 200$, the peak total shear stress gradually rises to about $1.1\tau_w$ at $Re_\theta = 500$, where transition is near completion. From $Re_\theta = 500$ to 800 the overshoot gradually decreases, but the minor excess over wall shear stress persists well into the turbulent region.

In the present flow, the early transitional region is from the inlet of $Re_\theta = 80$ at $x = 0$ to approximately $Re_\theta = 180$ corresponding to $x = 700\theta_0$. In this simulation, the streamwise pressure gradient is kept to nearly zero, which results in a slightly perturbed laminar boundary layer in this region with minimal deviation from the Blasius profile. For example, we have seen that the relative drift of the mean skin-friction coefficient away from the analytical Blasius solution is less than 1 %. We found that in the early transitional region, the mean velocity profiles differ from their corresponding Blasius solutions by no more than $0.7\,\%U_\infty$. Figure 29 shows that in the early transitional region, the peak locations of u'_{rms} scale with the Blasius coordinate η.

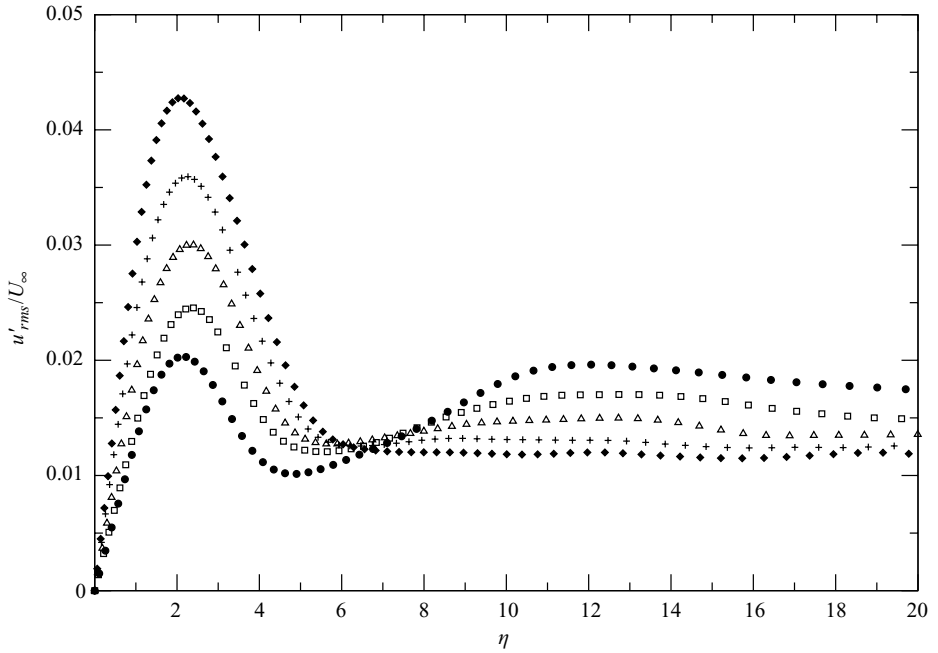

FIGURE 29. u'_{rms}/U_∞ as a function of $\eta = y(U_\infty/\nu x)^{1/2}$ in the early transitional region. Circle, $Re_\theta = 100$; box, $Re_\theta = 120$; triangle, $Re_\theta = 140$; plus, $Re_\theta = 160$; diamond, $Re_\theta = 180$.

3.5. *Transition mechanism*

Full three-dimensional DNS velocity data fields collected sequentially from $100\mathscr{T}$ to $101\mathscr{T}$ at a time interval of $0.05\mathscr{T}$ are used here to address bypass transition mechanism questions; the most important of these concern the location and cause of the breakdown event.

Figure 30 shows the decay of free stream disturbance as the initially isotropic turbulent patch is convected over the plate using spanwise-averaged turbulence intensities as a function of streamwise coordinate and time. In this figure, the intensity level drops from 5 % near the inlet to slightly less than 2 % near the exit. These phase-dependent disturbance levels do not have exactly the same meaning as the time-averaged intensity levels used in continuous free stream turbulence studies because of the highly localized nature of the present disturbances. The time-averaged free stream turbulence intensity level at $Re_\theta = 900$ is only 0.6 % as indicated by figure 14.

It is of interest to clarify the role of Tollmien–Schlichting waves, if any, in the present laminar boundary layer. Figure 31 shows the wall-normal distribution of u'_{rms} at two x-stations very close to the inlet for the instant of $100.1\mathscr{T}$. As also shown in the figure by the experimental data of Schubauer & Skramstad (1947), if Tollmien–Schlichting waves were dominant in the laminar boundary layer, u'_{rms} would have exhibited a near-wall peak below $y = \delta^*$ and a much lower secondary peak at $y \approx 3\delta^*$. Between the primary and secondary peaks u'_{rms} dips to a minimum close to zero. The DNS profiles presented in figure 31 cannot be attributed to Tollmien–Schlichting waves. As shown in the remainder of this section, the present boundary layer transitions through a bypass route.

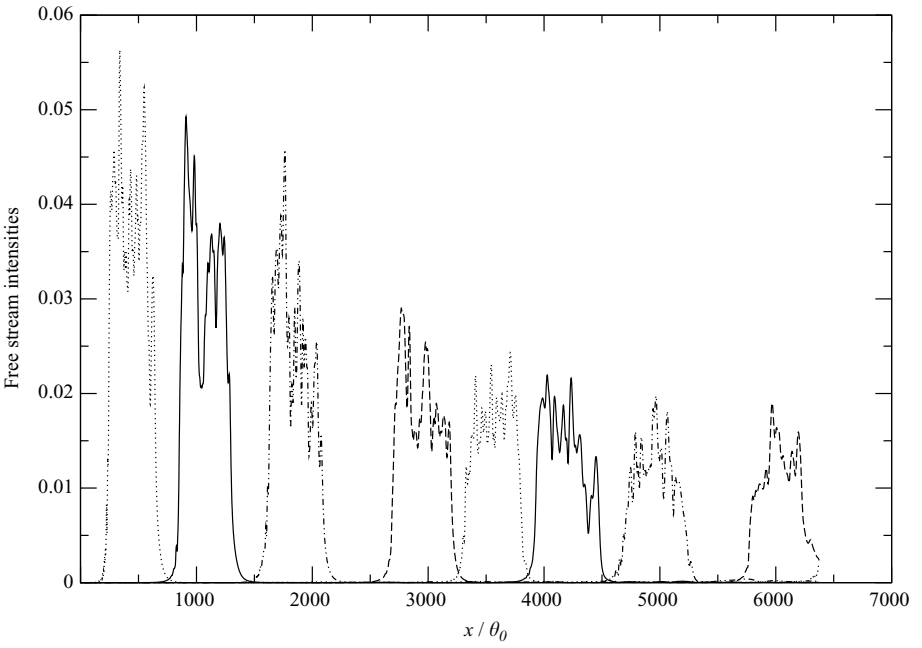

FIGURE 30. Decay of spanwise-averaged free stream turbulence intensities as a function of streamwise coordinate x/θ_0 at the wall-normal location of $y/\theta_0 = 281$ (see also figure 1 for the slab locations at different instants). Solid line, u'_{rms}/U_∞ at $100.4\mathscr{T}$; dashed line, u'_{rms}/U_∞ at $100.0\mathscr{T}$; dotted line, v'_{rms}/U_∞ at $100.3\mathscr{T}$; dash-dotted-dotted line, w'_{rms}/U_∞ at $100.65\mathscr{T}$.

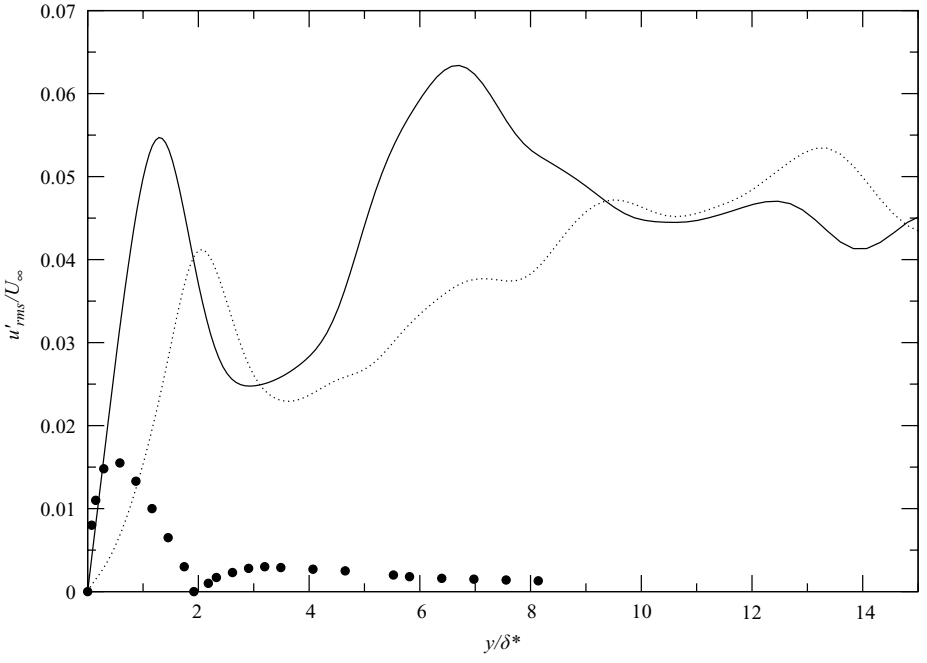

FIGURE 31. Spanwise-averaged streamwise turbulence intensity u'_{rms}/U_∞ in the early transitional region at $t = 100.1\mathscr{T}$ as a function of wall-normal coordinate, y/δ^*. Solid line, at $Re_\theta = 100$; dotted line, at $Re_\theta = 120$; circle, a typical distribution of Tollmien–Schlichting wave from Schubauer & Skramstad (1947).

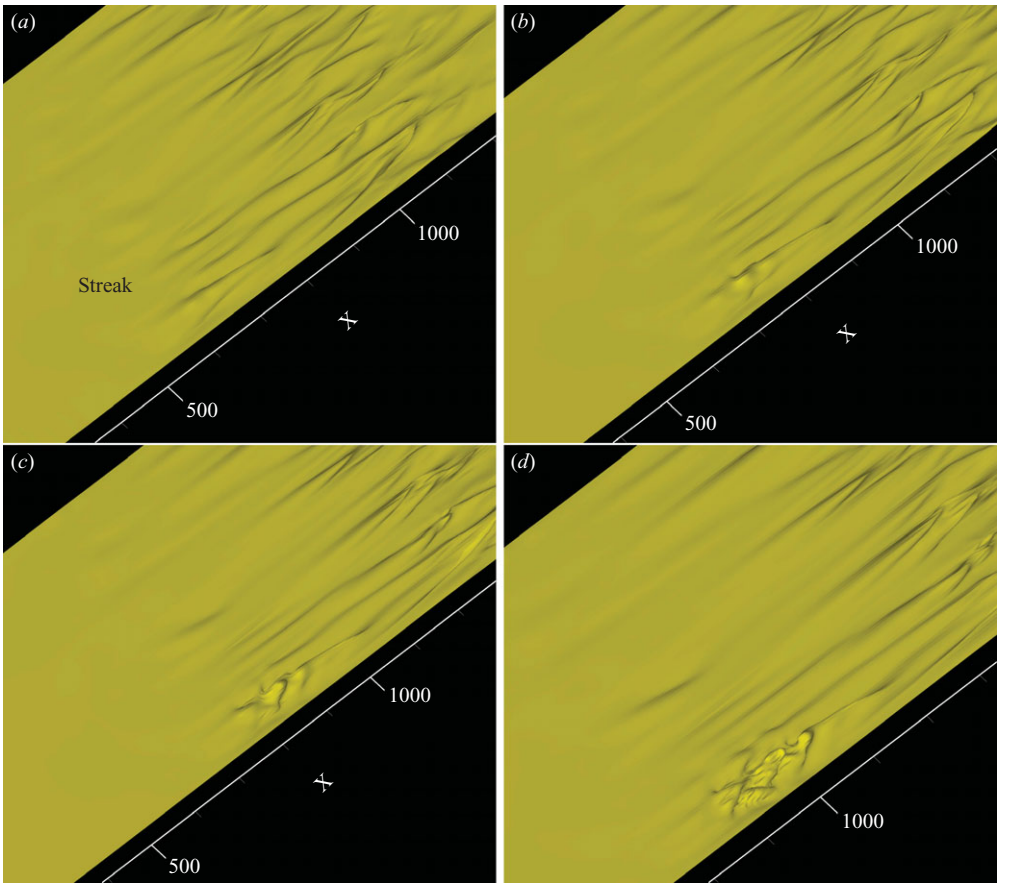

FIGURE 32. Iso-surfaces of $u/U_\infty = 0.8$ at four consecutive instants showing the time and streamwise location of breakdown. (*a*) $t = 100.45\mathscr{T}$; (*b*) $100.5\mathscr{T}$; (*c*) $100.55\mathscr{T}$ (immediately before breakdown); (*d*) $100.6\mathscr{T}$ (breakdown).

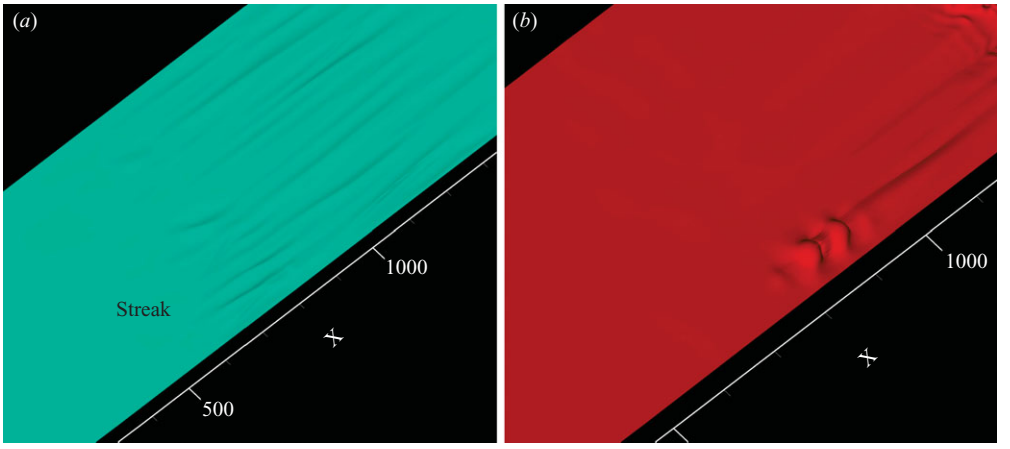

FIGURE 33. Iso-surfaces of u at the instant of $100.55\mathscr{T}$ immediately prior to breakdown. (*a*) Deep inside the boundary layer with $u/U_\infty = 0.3$; (*b*) near the boundary layer edge with $u/U_\infty = 0.99$.

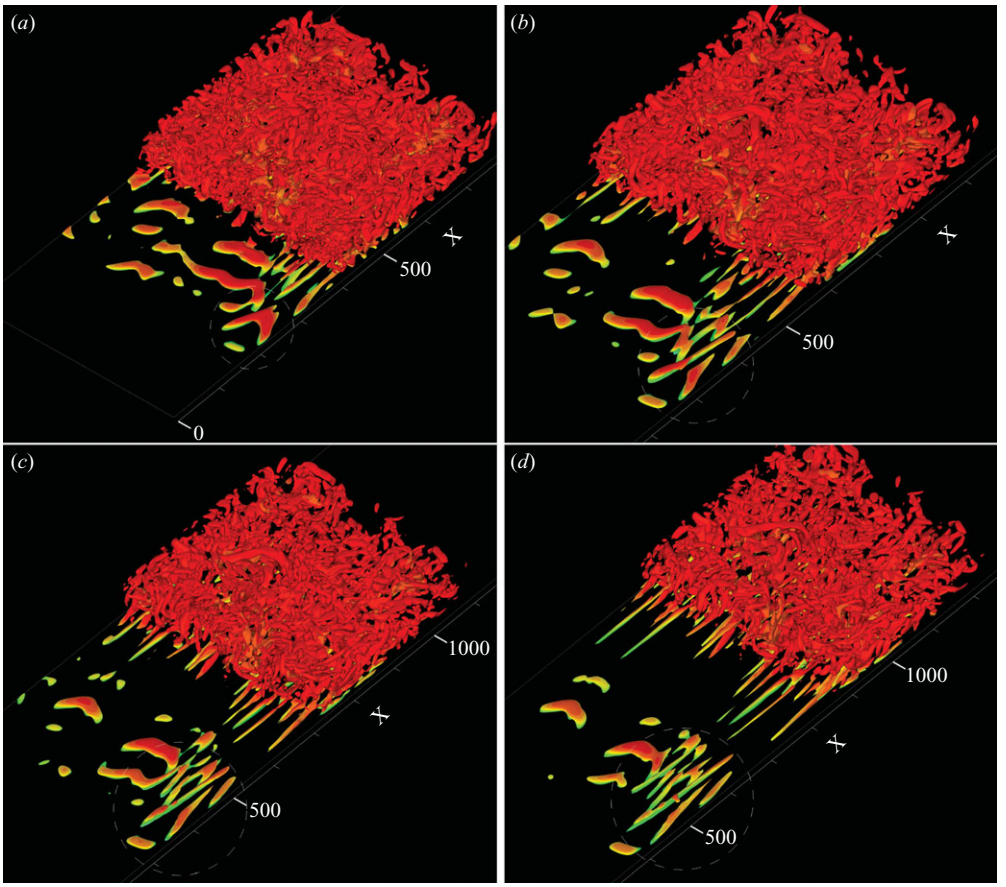

FIGURE 34. For legend see facing page.

The iso-surfaces of u presented in figure 32 suggest that breakdown event within this cycle occurs at the instant of $100.6\mathscr{T}$ over the streamwise region of $850 < x/\theta_0 < 1100$. These iso-surfaces are generally cone-shaped with tips in the downstream end. A bulge in the iso-surface corresponds to low streamwise momentum being transported away from the wall, i.e. negative u' at the local elevation. As shown in figure 33, immediately prior to breakdown ($t = 100.55\mathscr{T}$) the iso-surfaces of $u = 0.99U_\infty$ (at the boundary layer edge) exhibit a number of aligned bulges in the streamwise direction, corresponding to a local pattern of alternating negative and positive u' near the boundary layer edge.

The aligned bulges in the iso-surfaces of u at the boundary layer edge are related to the heads of three hairpin vortices in a packet. From figures 3(a) and 34, it is clear that a Λ-shaped vortex structure has been formed inside the boundary layer at $100.25\mathscr{T}$ from a receptivity process. The two leg elements of the Λ structure develop into two oblique quasi-streamwise vortices at $100.35\mathscr{T}$ with the disappearing of the middle joint portion of the Λ. A packet of three hairpin vortices emerges out of this quasi-streamwise vortex pair at $100.5\mathscr{T}$ and $100.55\mathscr{T}$. Breakdown follows at $100.6\mathscr{T}$. Figure 34 also clearly shows that at the same time when the hairpin packet is being developed, a number of new Λ structures also gradually emerge in different areas of the flow out of quasi-spanwise structures.

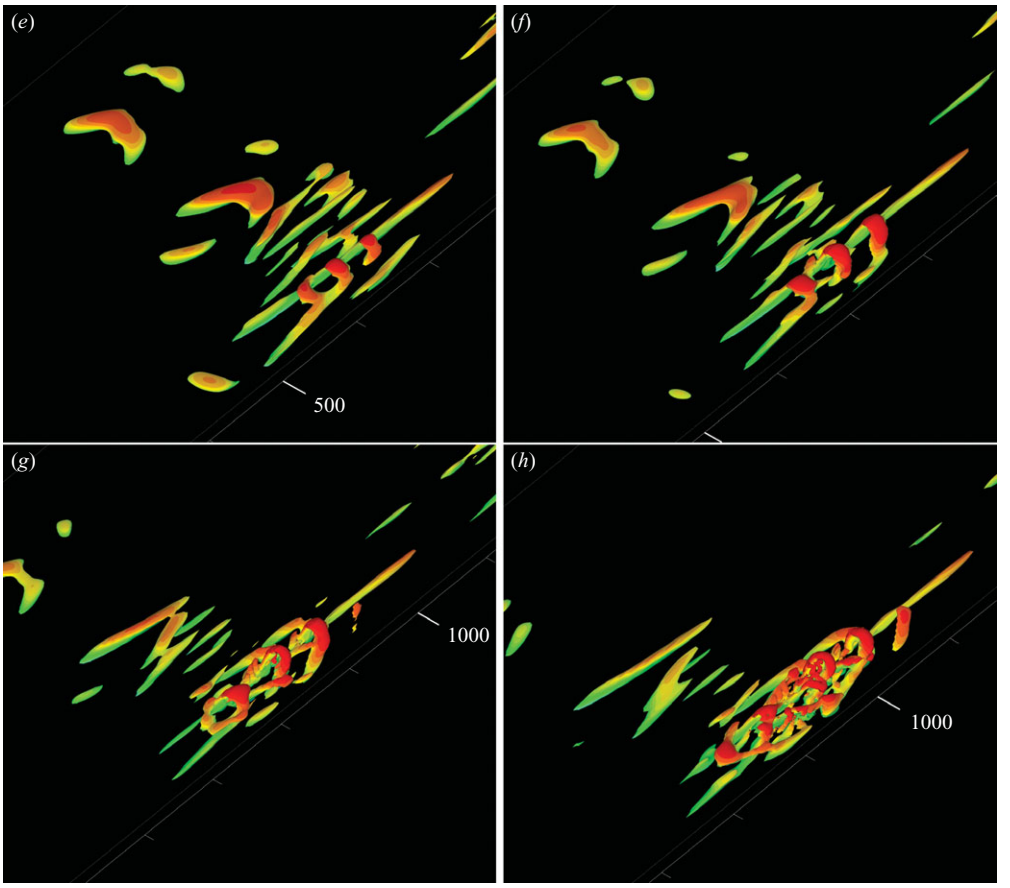

FIGURE 34. Iso-surfaces of the second invariant of the velocity gradient tensor at eight consecutive instants showing the vortex structures before and during breakdown. The iso-surfaces are coloured based on local values of u with higher u represented by red, $0 \leqslant u \leqslant 1.0$. (*a*) $t = 100.25\mathscr{T}$; (*b*) $100.3\mathscr{T}$; (*c*) $100.35\mathscr{T}$; (*d*) $100.4\mathscr{T}$; (*e*) $t = 100.45\mathscr{T}$; (*f*) $t = 100.5\mathscr{T}$; (*g*) $t = 100.55\mathscr{T}$; (*h*) $t = 100.6\mathscr{T}$.

The bypass transition mechanism observed in the present ZPGFPBL is similar to observations in several previous studies of spatially developing laminar boundary layer under localized disturbances. Acarlar & Smith (1987) reported experimental evidence of hairpin vortices resulting from continuous injection of fluid from the wall into a laminar boundary layer. Chaotic structures developed subsequent to the formation of the hairpins. Low-speed streak-like structures were observed between the legs of the hairpin vortices. Singer & Joslin (1994) performed spatially developing DNS of a laminar boundary layer under localized wall-normal fluid injection. An initial vortex was triggered by the injection. The legs of the vortex were stretched into a hairpin shape as it is convected downstream. Multiple hairpin vortex heads developed between the stretched legs, which eventually resulted in a young turbulent spot. A more recent related work was reported by Kim, Sung & Adrian (2008).

Several previous studies on laminar boundary layer under the perturbation of continuous free stream turbulence emphasized on the role of elongated negative u'

structures (streaks), e.g. Jacobs & Durbin (2001), Brandt *et al.* (2004) and Zaki & Durbin (2005). Streaks are abundant in the present ZPGFPBL prior to breakdown (see figures 32 and 33). These cone-shaped streaks appear to be the result of the transport of low streamwise momentum fluid away from the wall by quasi-streamwise vortices as they convect downstream. Based on flow visualizations in the present ZPGFPBL, the streaks appear to be merely a kinematic feature (symptom); the nonlinear dynamical development of Λ-shaped vortices into hairpin packets is responsible for the breakdown of the Blasius layer.

4. Concluding remarks

We have taken a Blasius layer from $Re_\theta = 80$ through transition to a low-Reynolds-number turbulent ZPGFPBL in a well-controlled manner. The quality of the simulation is manifested by the close adherence of the statistics including skin friction over an extended early transitional region to the Blasius solution, and good agreement with a number of classical experimental datasets in the turbulent region. The perturbation introduced for promotion of transition is weak, intermittent and leaves faint footprints on the downstream ZPGFPBL. The full velocity field of the isotropic turbulence patch introduced in the free stream at $Re_\theta = 80$ is available in raw form so that the inflow condition is precisely defined and repeatable without ambiguity. The discovered minor overshoot of total shear stress has not been reported before. It is contrary to the common belief that total shear stress varies monotonically with wall distance in a spatially developing, low-Reynolds-number ($Re_\theta < 1000$ in this case) turbulent ZPGFPBL. It is quite obvious that this overshoot is a residual effect of boundary layer transition and may gradually diminish as the ZPGFPBL develops further downstream. It is notable that the overshoot was absent in previous ZPGFPBL simulations using rescaling procedures or periodic boundary condition in the streamwise direction. It is well known that laboratory low-Reynolds-number turbulent ZPGFPBLs are affected by the actual low value of the Reynolds number, and by the type of tripping device used. A case in point is the work of Erm & Joubert (1991) in which a series of experiments were performed to demonstrate such influences. Our observed total shear stress overshoot in the turbulent region is a diminishing effect of transition, and is unlikely to persist in fully developed turbulent boundary layers.

Breakdown in the present ZPGFPBL bypass transition is due to the hairpin packets arising from the obliquely oriented legs of upstream disjointed Λ vortices. This mechanism is consistent with a number of previous experimental and numerical studies of spatially developing laminar boundary layer under localized perturbations in the wall region. This mechanism also bears similarity to the secondary instabilities in boundary layer natural transition (Herbert 1988). Bypass transition was defined as the primary instability in natural transition, i.e. the Tollmien–Schlichting mechanism is bypassed. It is logical to expect, as indeed in the present ZPGFPBL, that a well-controlled bypass transition will proceed along a path broadly resembling one of the secondary instabilities in natural transition.

The striking preponderance of hairpin vortical structures in the limited flow visualizations presented in this paper suggests that an in-depth study on the time-dependent dynamics of the turbulent ZPGFPBL should be fruitful. This is the first time that direct evidence (in the form of a *solution* of the Navier–Stokes equations, obeying the statistical measurements, as opposed to synthetic superposition of the structures) shows such dominance of these structures. Specifically, it would be

interesting to study any possible connections between the hairpin vortices and possible large and very-large scale motions in a ZPGFPBL such as those observed indirectly in the experiments of Adrian *et al.* (2000) and Hutchins & Marusic (2007). This may require an extension of the computational domain streamwisely for the ZPGFPBL to reach $Re_\theta \approx 2000$. Additionally, it would be important to understand the underlying reasons for the vivid appearance of these structures and its relation to the specific prescription of the inflow conditions in the present simulation.

The present computational statistics have been posted on the Stanford University Centre for Turbulence Research web site (http://ctr.stanford.edu) for public access. The isotropic turbulence slab used for inflow perturbation is available on compact disk through e-mail request. A sequence of 20 three-dimensional instantaneous velocity fields is also available for user-supplied external hard-drive.

The computer program used in this study was developed by the late Dr Charles D. Pierce of the centre for Turbulence Research at Stanford. This work was supported by the Department of Energy's ASC Program, NSERC Discovery Grant, Department of Defense Academic Research Program and the Canada Research Chair Program. The simulations were performed on the IBM terascale parallel machines at the San Diego Supercomputing centre. We thank Professor Peter Bradshaw for his very detailed comments on the entire manuscript. We also thank Dr Philippe Spalart for his comments on figures 18 and 28.

REFERENCES

Acarlar, M. S. & Smith, C. R. 1987 A study of hairpin vortices in a laminar boundary layer. Part 2. Hairpin vortices generated by fluid injection. *J. Fluid Mech.* **175**, 43–83.

Adrian, R. J., Meinhart, C. D. & Tomkins, C. D. 2000 Vortex organization in the outer region of the turbulent boundary layer. *J. Fluid Mech.* **422**, 1–54.

Alfredsson, P. H., Johansson, A. V., Haritonidis, J. H. & Eckelmann, H. 1988 The fluctuation wall-shear stress and the velocity field in the viscous sublayer. *Phys. Fluids* **31**, 1026–1033.

Barenblatt, G. I. & Chorin, A. J. 1998 Scaling of the intermediate region in wall-bounded turbulence: the power law. *Phys. Fluids* **10**, 1043–1044.

Brandt, L., Schlatter, P. & Henningson, D. S. 2004 Transition in boundary layers subject to free-stream turbulence. *J. Fluid Mech.* **517**, 167–198.

Chakraborty, P., Balachandar, S. & Adrian, R. 2005 On the relationships between local vortex identification schemes. *J. Fluid Mech.* **535**, 189–214.

Choi, H. & Moin, P. 1990 On the space–time characteristics of wall-pressure fluctuations. *Phys. Fluids* **2**, 1450–1460.

Coles, D. 1956 The law of the wake in the turbulent boundary layer. *J. Fluid Mech.* **1**, 191–226.

DeGraaff, D. B. & Eaton, J. K. 2000 Reynolds-number scaling of the flat-plate turbulent boundary layer. *J. Fluid Mech.* **422**, 319–346.

Erm, L. P. & Joubert, P. N. 1991 Low Reynolds number turbulent boundary layers. *J. Fluid Mech.* **230**, 1–44.

Erm, L. P., Smits, A. J. & Joubert, P. N. August 7–9, 1985 Low Reynolds number turbulent boundary layers on a smooth flat surface in a zero pressure gradient. In *Proceedings of fifth Symposium on Turbulent Shear Flows*, Ithaca, NY.

Favre, A. J., Gaviglio, J. J. & Dumas, R. J. 1957 Space–time double correlations and spectra in a turbulent boundary layer. *J. Fluid Mech.* **2**, 313–342.

Head, M. R. & Bandyopadhyay, P. 1981 New aspects of turbulent boundary layer structure. *J. Fluid Mech.* **107**, 297–338.

Herbert, T. 1988 Secondary instability of boundary layers. *Annu. Rev. Fluid Mech.* **20**, 487–526.

Honkan, A. & Andreopoulos, Y. 1997 Vorticity, strain-rate and dissipation characteristics in the near-wall region of turbulent boundary layers. *J. Fluid Mech.* **350**, 29–96.

Hunt, J. C. R., Wray, A. A. & Moin, P. 1988 Eddies, streams, and convergence zones in turbulent flows. In *Proceedings of Summer Program*, pp. 9–14. Centre for Turbulence Research, Stanford University.

Hutchins, N., Hambleton, W. T. & Marusic, I. 2005 Inclined cross-stream stereo particle image velocimetry measurements in turbulent boundary layers. *J. Fluid Mech.* **541**, 21–54.

Hutchins, N. & Marusic, I. 2007 Evidence of very long meandering features in the logarithmic region of turbulent boundary layers. *J. Fluid Mech.* **579**, 1–28.

Jacobs, R. G. & Durbin, P. A. 2001 Simulation of bypass transition. *J. Fluid Mech.* **428**, 185–212.

Khurajadze, G. & Oberlack, M. 2004 DNS and scaling laws from new symmetry groups of zpg turbulent boundary layer flow. *Theor. Comput. Fluid Dyn.* **18**, 391441.

Kim, J., Moin, P. & Moser, R. D. 1987 Turbulence statistics in fully developed channel flow at low Reynolds number. *J. Fluid Mech.* **177**, 133–166.

Kim, K., Sung, H. J. & Adrian, R. J. 2008 Effects of background noise on generating coherent packets of hairpin vortices. *Phys. Fluids* **20**, 105107.

Lund, T. S., Wu, X. & Squires, K. D. 1998 Generation of turbulent inflow data for spatially-developing boundary layer simulations. *J. Comput. Phys.* **140**, 233–258.

Moin, P. & Kim, J. 1985 The structure of the vorticity field in turbulent channel flow. Part 1. Analysis of instantaneous fields and statistical correlations. *J. Fluid Mech.* **155**, 441–464.

Monkewitz, P., Chauhan, K. A. & Nagib, H. M. 2007 Self-consistent high-Reynolds-number asymptotic for zero-pressure-gradient turbulent boundary layers. *Phys. Fluids* **19**, 115101.

Murlis, J., Tsai, H. M. & Bradshaw, P. 1982, The structure of turbulent boundary layers at low Reynolds numbers. *J. Fluid Mech.* **122**, 13–56.

Nagib, H. M., Chauhan, K. & Monkewitz, P. 2007 Approach to an asymptotic state for zero pressure gradient turbulent boundary layers. *Phil. Trans. R. Soc.* A **365**, 755–770.

Ovchinnikov, V., Piomelli, U. & Choudhari, M. M. 2006 Numerical simulations of boundary-layer transition induced by a cylinder wake. *J. Fluid Mech.* **547**, 413–441.

Pauley, L. L., Moin, P. & Reynolds, W. C. 1990 The structure of two-dimensional separation. *J. Fluid Mech.* **220**, 397–411.

Perry, A. E. & Chong, M. S. 1982 On the mechanism of wall turbulence. *J. Fluid Mech.* **119**, 173–217.

Perry, A. E., Henbest, S. & Chong, M. S. 1986 A theoretical and experimental study of wall turbulence. *J. Fluid Mech.* **165**, 163–200.

Pierce, C. D. & Moin, P. 2001 Progress variable approach for large-eddy simulation of turbulent combustion. *Report No.* TF-80, Stanford University.

Pierce, C. D. & Moin, P. 2004 Progress variable approach for large-eddy simulation of non-premixed turbulent combustion. *J. Fluid Mech.* **504**, 73–97.

Purtell, L. P., Klebanoff, P. S. & Buckley, F. T. 1981 Turbulent boundary layer at low Reynolds number. *Phys. Fluids* **24**, 802–811.

Rai, M. M. & Moin, P. 1993 Direct numerical simulation of transition and turbulence in a spatially evolving boundary layer. *J. Comput. Phys.* **109**, 169–192.

Roach, P. E. & Brierley, D. H. 1990 The influence of a turbulent frees-stream on zero pressure gradient transitional boundary layer development. Part I. Test Cases T3A and T3B. In *Numerical Simulation of Unsteady Flows and Transition to Turbulence*, pp. 319–347, Cambridge University Press.

Robinson, S. K. 1991 Coherent motion in the turbulent boundary layer. *Annu. Rev. Fluid Mech.* **23**, 601–639.

Schubauer, G. B. & Skramstad, H. K. 1947 Laminar boundary layer oscillations and stability of laminar flow. *J. Aero. Sci.* **14**, 69–78.

Singer, B. A. & Joslin, R. D. 1994 Metamorphosis of a hairpin vortex into a young turbulent spot. *Phys. Fluids* **11**, 3724–3736.

Smith, R. W. 1994 Effect of Reynolds number on the structure of turbulent boundary layers. PhD thesis, Department of Mechanical and Aerospace Engineering, Princeton University.

Spalart, P. R. 1988 Direct simulation of a turbulent boundary layer up to $R_\theta = 1410$. *J. Fluid Mech.* **187**, 61–98.

Spalart, P. R. & Watmuff, J. H. 1993 Experimental and numerical study of a turbulent boundary layer with pressure gradients. *J. Fluid Mech.* **249**, 337–371.

Tomkins, C. D. & Adrian, R. J. 2003 Spanwise structure and scale growth in turbulent boundary layers. *J. Fluid Mech.* **490**, 37–74.

Turan, O., Azad, R. S. & Kassab, S. Z. 1987 Experimental and theoretical evaluation of the k_1^{-1} spectral law. *Phys. Fluids* **30**, 3463–3474.

Willmarth, W. W. 1975 Pressure fluctuations beneath turbulent boundary layers. *Annu. Rev. Fluid Mech.* **7**, 13–38.

Wu, X., Jacobs, R., Hunt, J. C. R. & Durbin, P. A. 1999 Simulation of boundary layer transition induced by periodically passing wakes. *J. Fluid Mech.* **398**, 109–153.

Wu, X. & Moin, P. 2008 A direct numerical simulation study on the mean velocity characteristics in turbulent pipe flow. *J. Fluid Mech.* **608**, 81–112.

Zagarola, M. & Smits, A. J. 1998 A new mean velocity scaling for turbulent boundary layers. In *Proceedings of ASME Fluids Engineering Division Summer Meeting*, June 21–25, Washington DC.

Zaki, T. A. & Durbin, P. A. 2005 Mode interaction and the bypass route to transition. *J. Fluid Mech.* **531**, 85–111.